Performance and limits of a shallow-water model for landslide-generated tsunamis: from laboratory experiments to simulations of flank collapses at Montagne Pelée (Martinique)

P Poulain, A Le Friant, A Mangeney, S. Viroulet, E Fernandez-Nieto, M Castro Diaz, Marc Peruzzetto, Gilles Grandjean, François Bouchut, Rodrigo Pedreros, et al.

HAL Id: hal-03974933
https://brgm.hal.science/hal-03974933

Performance and limits of a shallow-water model for landslide-generated tsunamis: from laboratory experiments to simulations of flank collapses at Montagne Pelée (Martinique)

P. Poulain [1], A. Le Friant,[1] A. Mangeney,[1] S. Viroulet,[1,2] E. Fernandez-Nieto,[3] M. Castro Diaz,[4] M. Peruzzetto [1,5] G. Grandjean,[5] F. Bouchut,[6] R. Pedreros[5] and J-C. Komorowski [1]

[1]*Université Paris Cité, Institut de Physique du Globe de Paris, departements of volcanic systems and sismology, CNRS, F-75005 Paris, France. E-mail: poulainpablo@gmail.com*
[2]*Institut de Mécanique des Fluides de Toulouse (IMFT) - Université de Toulouse, CNRS, 31400 Toulouse, France*
[3]*Dpto. Matematica Aplicada I, ETS Arquitectura - Universidad de Sevilla, Avda. Reina Mercedes S/N, 41012 Sevilla, Spain*
[4]*Departamento de Analisis Matematico, Estadística e Investigación Operativa y Matemática Aplicada. Universidad de Malaga, Facultad de Ciencias, Campus Teatinos S/N, 29081 Málaga, Spain.*
[5]*BRGM (French Geological Survey), Orléans, France*
[6]*Laboratoire d'Analyse et de Mathématiques Appliquées (UMR 8050), CNRS, Univ. Gustave Eiffel, UPEC, F-77454, Marne-la-Vallée, France*

SUMMARY

We investigate the dynamics and deposits of granular flows and the amplitude of landslide-generated water waves using the HySEA depth-averaged shallow-water numerical model, both at laboratory and field scales. We evaluate the different sources of error by quantitatively comparing the simulations with (i) new laboratory experiments of granular collapses in different conditions (dry, immersed, dry flow entering water) and slope angles and (ii) numerical simulations made with the SHALTOP code that describes topography effects better than most depth-averaged landslide-tsunami models. For laboratory configurations, representing the limits of the shallow-water approximation in such models, we show that topography and non-hydrostatic effects are crucial. When topography effects are accounted for empirically—by artificially increasing the friction coefficient and performing non-hydrostatic simulations—the model is able to reproduce the granular mass deposit and the waves recorded at gauges located at a distance of more than two to three times the characteristic dimension of the slide with an error ranging from 1 to 25 per cent depending on the scenario, without any further calibration. Taking into account this error estimate, we simulate landslides that occurred on Montagne Pelée volcano, Martinique, Lesser Antilles as well as the generated waves. Multiple collapse simulations support the assumption that large flank collapses on Montagne Pelée likely occurred in several successive subevents. This result has a strong impact on the amplitude of the generated waves and thus on the associated hazards. In the context of the ongoing seismic volcanic unrest at Montagne Pelée volcano, we calculate the debris avalanche and associated tsunamis for two potential flank-collapse scenarios.

Key words: Numerical modelling; Tsunamis; Submarine landslides; Volcanic arc processes; Volcanic hazards and risks.

1 INTRODUCTION

Volcano flank collapses are recurrent processes that are part of the evolution of a volcanic edifice (Siebert 1984; McGuire 1996). These gravity induced mass movements and debris avalanches can trigger tsunamis (e.g. Kelfoun *et al.* 2010; Abadie *et al.* 2012, Gylfadottir *et al.* 2017; Barrett *et al.* 2019; Williams *et al.* 2019; Perttu *et al.* 2020; Paris *et al.* 2020).

The dynamics of these natural granular flows and thus the generation of the tsunami is still an open issue (e.g. Yavari-Ramshe & Ataie Ashtiani 2016). Numerical simulations provide a unique tool to quantify these processes (see Yavari-Ramshe *et al.* 2015; Behrens *et al.* 2021, for a review). However, significant uncertainties have to be taken into account in the simulation of landslide-generated tsunamis regarding (i) the position and characteristics of the released mass, (ii) the estimation of sources probabilities (Lane *et al.* 2016; Løvholt *et al.* 2020), (iii)

the rheological laws and parameters to be used in the simulations and (iv) the inevitable approximations made in the physically based model. Each of these uncertainties is a source of active research.

Uncertainties regarding the initial conditions, the material composition (de Haas *et al*. 2015), the rheological laws and associated parameters (Delannay *et al*. 2017; Peruzzetto *et al*. 2020) can be addressed by running multiple simulations (Løvholt *et al*. 2020), requiring huge computational efforts. Simplified depth-averaged models are thus often used for field-scale studies even if they are less accurate than full 3-D models (Gittings 1992; Abadie *et al*. 2008; Horrillo *et al*. 2013; Ma *et al*. 2013). Simplified models are based on the so-called thin-layer approximation for the landslide and shallow-water or long-wave approximation for the tsunami: the landslide thickness, respectively water depth, is assumed to be small in comparison with the landslide downslope extension, respectively, tsunami wavelength. Since the pioneering work of Savage & Hutter (1989), depth-averaged landslide-tsunami models have seen significant developments (Gittings 1992; Mangeney *et al*. 2000; Fernandez-Nieto *et al*. 2008; Abadie *et al*. 2010; Kelfoun 2011; Kelfoun & Vargas 2015). There are still however a number of mathematical, mechanical and numerical shortcomings in these models that, when not appropriately addressed, may induce significant error in the simulation.

In this work, we focus on part of these modelling challenges and on quantifying the effect of their accurate implementation. We know there is presently no model for landslide-generated tsunamis that accurately deals with all the aspects described below at a reasonable computational cost and no precise idea of the errors made when neglecting some of them. Despite strong differences between models, most studies conclude that their model well reproduces laboratory experiments or field data. We believe that a key point for future model improvement is to show, quantify and analyse uncertainties to reduce bias in modelling.

A major modelling challenge, that we will further call *topography effects*, concerns the accurate derivation of thin-layer depth-averaged equations for granular flows for a general 2-D topography $b(x, y)$ (Peruzzetto *et al*. 2021). This derivation induces two related difficulties: (1) complex terms linked to topography curvature have to be taken into account and (2) the thin-layer approximation and depth-averaging should be done in a reference frame following the topography.

The first rigorous derivations of depth-averaged flow equations over arbitrary topographies, with a curvature small enough to be compatible with the thin-layer approximation, were provided by Bouchut *et al*. (2003) and Bouchut & Westdickenberg (2004) for a 1-D and 2-D topography, respectively, and solved numerically by Mangeney-Castelneau *et al*. (2005) and Mangeney *et al*. (2007a) in the SHALTOP code. In the resulting equations, two curvature terms appear: one ensures that the flow velocity remains tangent to the topography (as assumed for thin-layer models) and the other appears when frictional rheologies are used. To our knowledge, only a few landslide models accurately account for these effects. Only the curvature term related to friction is included in the RAMMS code (Christen *et al*. 2010; Fischer *et al*. 2012) while in FOAM, Rauter & Tukovic (2018) and Rauter *et al*. (2018) take curvature terms into account implicitly by solving numerically for the bottom pressure. As there is no model for landslide-generated tsunamis accounting for curvature effects, we will use SHALTOP here to (i) estimate the error in landslide dynamics and deposits estimated by models simulating both the landslide and the tsunami without properly accounting for topography effects and (ii) calibrate the models to artificially reduce this error.

A related challenge, poorly addressed in the literature, is the different coordinate systems that have to be considered to describe the landslide and the tsunami. Indeed, to accurately derive the thin-layer or shallow-water approximation, it is necessary to measure the thickness of the material involved in the direction roughly normal to the surface of the considered thin flow. Thus, the shallow approximation should be imposed in a Cartesian horizontal/vertical frame for the tsunami part and in a coordinate system adapted to the topography variations for the landslide part as stated above. Very few models consider two different coordinates systems (Ma *et al*. 2015; Delgado-Sanchez *et al*. 2020) and none account for topography curvature. While the Volcflow model (Kelfoun *et al*. 2010) uses a topography-related reference frame for both the tsunami and landslide parts, the D-Claw model (George *et al*. 2017) uses Cartesian horizontal/vertical coordinates for both parts, as in the HySEA code used here. The introduction of non-hydrostatic terms in the equations [Garres-Diaz *et al*. 2020; eq. (4.9) in Bouchut *et al*. 2016a] helps reduce the error related to inappropriate coordinate systems (Delinger & Iverson 2004; Zhang *et al*. 2021a; Garres-Diaz *et al*. 2020). But additional considerations must also be taken into account in the modelling.

The third challenge is to describe grain-fluid interactions and dilatancy in landslides. Depth-averaged thin-layer landslide models have recently been improved to partly take into account these interactions (Pitman & Lee 2005, Pudasaini 2012; Mergili *et al*. 2017), in particular dilatancy and associated pore fluid pressure effects (Iverson & George 2014; Bouchut *et al*. 2016b, 2017; Pudasaini & Mergili 2019). However, these models contain several parameters that are difficult to estimate for field applications and, in their present state, do not accurately describe the curvature of complex topographies. In the simulation of tsunamis generated by landslides, the moving mass is commonly considered as a simplified grain–fluid mixture, where fluid effects are reduced to buoyancy and drag between the granular layer and the water layer, without dilatancy effects (Fernandez-Nieto *et al*. 2008; Yavari-Ramshe *et al*. 2015; Ma *et al*. 2015, Zhang *et al*. 2021b). The main advantage of these models is to involve only a few parameters. This is in particular the case for the HySEA model (Macias *et al*. 2021b) that will be used in this work.

The fourth challenge concerns the coupling strategy between the landslide flow and tsunami generation. A first approach considers the combination of the landslide and water as a single layer containing a mixture (the grain-water mass is considered as an effective media; George *et al*. 2017) or a multiphase fluid (the grain and fluid equations are both solved; Horrillo *et al*. 2013; Grilli *et al*. 2014; Tappin *et al*. 2014). A second strategy is to couple models dealing with the different processes: granular flow along the slope, tsunami generation and tsunami propagation (Abadie *et al*. 2012; Kim *et al*. 2019). A third approach, used in our study, considers the granular flow and the water as two separate layers that are coupled through friction between the two layers as in HySEA (Fernandez-Nieto *et al*. 2008; Macias *et al*. 2021b).

Finally, different level of approximation can be made for the landslide and tsunami description. Lots of models solve shallow-water (or thin-layer) depth-averaged equations, assuming hydrostatic pressure for both the granular and water layers (Jiang & LeBlond 1992; Heinrich *et al*. 1998; Mangeney *et al*. 2000; Majd & Sanders 2014; Fine *et al*. 2003, 2005; Fernandez-Nieto *et al*. 2008; Yavari-Ramshe & Ataie-Ashtiani 2015). These models suffer from the lack of dispersion in tsunami propagation, potentially leading to significant bias. Indeed, wave dispersion can be significant (Glimsdal *et al*. 2013; Ma *et al*. 2015) when the water wavelength is smaller than or about the same order of magnitude as the water depth (Yavari-Ramshe & Ataie-Ashtiani 2016). For more than two decades, more advanced depth-averaged models to describe water wave propagation have been developed based on Boussinesq-type equations (non-hydrostatic pressure), that are weakly or fully dispersive (Kirby *et al*. 1998; Zhou *et al*. 2011; Shi *et al*. 2012; Popinet 2015; Kirby *et al*. 2022), as is the case for the HySEA model (Macias *et al*. 2021b). Such depth-averaged non-hydrostatic models are also valid only for a sufficiently small ratio of the water depth to the tsunami wavelength, a limitation inadequately discussed in the literature (Macias *et al*. 2021a).

The error when using HySEA and the performance and shortcomings of these types of models will be estimated here by comparing simulations with (i) results from the landslide model SHALTOP better describing topography effects but not the water wave and (ii) eight laboratory experiments for dry, immersed and dry entering water initial configurations. These experiments are conducted in what can be considered to be the worst situations (strong slope variations, non-shallowness of part of the flow, conditions beyond the limits of the Boussinesq one-layer model, etc.), in order to quantify maximum errors. After estimating the error, we will apply the code to past volcanic flank collapses in Martinique for which we have geological data. Once calibrated on these events, we will use this model to preliminary estimate the impact of potential flank collapses related to the increasing volcanic activity of Montagne Pelée, Martinique, France (OVSM-IPGP 2019-2021). We will analyse these results in light of our study of the model limitations, in order to better understand the influence of the volume and morphology of the released mass, multiple-stage events, and the presence of a simplified erodible bed on the run-out distance and the emplacement of the deposits as well as on the generated water waves and their propagation.

In the next section, we first describe the HySEA and SHALTOP models. In Section 3, we present and compare the laboratory experiments and associated simulations of granular flows using the two models. In Section 4, we investigate Montagne Pelée flank collapses simulated with HySEA and discuss the results in Section 5.

2 NUMERICAL MODELS

To simulate tsunami generated by landslides, we use the HySEA code describing a grain–fluid layer flowing over a fixed bottom $z(x, y)$, with a water layer on top of it (Macias *et al*. 2021b). In HySEA, the shallow-water and thin-layer approximations as well as the flow averaging are done in a Cartesian horizontal/vertical reference frame for both the granular and the water layers. As described above, this assumption induces error that increases with the slope angle when it is applied to describe granular flow (Delgado-Sanchez *et al*. 2020). To quantify such error related to topography effects, we use the SHALTOP code describing dry granular flows over complex topographies, extended to account for buoyancy effects (see Section 2.3 for the granular rheology). In this way, we can quantify how much the friction parameters should be artificially increased in HySEA to roughly reproduce the deposit simulated when topography effects are appropriately taken into account.

Due to depth-averaging, these models assume that the flow is either completely mobile or static throughout its depth, which is not always the case, especially during the starting and the stopping phases (e.g. Ionescu *et al*. 2015; Martin *et al*. 2017) or if material is entrained or eroded (Iverson & Ouyang 2015). To approximate erosion processes in Section 5.2 for field application, we followed Moretti *et al*. (2012) by assuming that the static mass on the slope is just added to the flowing mass as the latter passes over the erodible bed. The velocity is then averaged over the whole mass depth (initially static mass and flowing mass). This oversimplified approach made it possible to quite well reproduce the dynamics of natural erosive flows when compared to seismic data. It is obviously less accurate than models describing both the static and flowing part in the granular avalanche (Fernandez-Nieto *et al*. 2016).

In HySEA and SHALTOP as in most landslide models, the water and the granular mass are assumed to be incompressible and homogeneous. Therefore, natural complexities such as density variations due to the expansion or contraction of the material and their impact on pore fluid pressure, segregation and fragmentation processes, or the incorporation of air and/or water are not taken into account, potentially leading to significant bias in the simulation (see Delannay *et al*. 2017, for a review and Rauter *et al*. 2022).

2.1 HYSEA numerical model

The two-layer HySEA code is a 2-D extension of the model proposed by Fernandez-Nieto *et al*. (2008), but using Cartesian coordinates and accounting for dispersion effects (i.e. non-hydrostatic) during water wave propagation. HySEA has been developed by the EDANYA group (Castro *et al*. 2005; Macias *et al*. 2015) and is based on an efficient hybrid finite-volume-finite-difference numerical scheme on GPU architectures (Macias *et al*. 2021a).

From the depth-averaged equations, the models solves the unknowns $(h_1, \mathbf{u}_1)$ and $(h_2, \mathbf{u}_2)$, representing the vertical height and horizontal velocity of the water and granular layer, respectively, averaged in the vertical z-direction. The velocities $\mathbf{u}_1$ and $\mathbf{u}_2$ are thus 2-D vectors in the horizontal (x, y) plane. Two additional unknowns are involved: the non-hydrostatic pressure p and the vertical velocity w_1, leading to Green–Naghdi equations (Green & Naghdi 1976) written as a non-hydrostatic pressure system. The mass and momentum balance equations

for the water and granular layers are:

$$\partial_t h_1 + \nabla \cdot (h_1 \mathbf{u}_1) = 0,$$

$$\partial_t \mathbf{u}_1 + \mathbf{u}_1 \cdot \nabla \mathbf{u}_1 + \nabla (g(b + h_1 + h_2) + p) + \frac{p}{h_1} \nabla \left(h_1 + \frac{3}{2}(b + h_2) \right) = S_{f,1},$$

$$\partial_t w_1 + \mathbf{u}_1 \cdot \nabla \ w_1 = \frac{3}{2} \frac{p}{h_1},$$

$$\nabla \cdot \mathbf{u}_1 + \frac{w_1 - \mathbf{u}_1 \cdot \nabla (b + h_2)}{h_1/2} = 0,$$

$$\partial_t h_2 + \nabla \cdot (h_2 \mathbf{u}_2) = 0,$$

$$\partial_t \mathbf{u}_2 + \mathbf{u}_2 \cdot \nabla \mathbf{u}_2 + \nabla \ (g(b + h_2) + g(1-)h_1) = S_{f,2} \tag{1}$$

with

$$S_{f,1} = \begin{cases} m_f \frac{h_2}{h_2 + r h_1} \parallel \mathbf{u}_2 - \mathbf{u}_1 \parallel (\mathbf{u}_2 - \mathbf{u}_1) \ \text{if} \ h_2 > 0, \\ -g \frac{n^2}{h_1^{4/3}} \parallel \mathbf{u}_1 \parallel \mathbf{u}_1 \qquad\qquad\qquad \text{if} \ h_2 = 0. \end{cases} \tag{2}$$

$$S_{f,2} = -(1-)m_f \frac{h_1}{h_2 + r h_1} \parallel \mathbf{u}_2 - \mathbf{u}_1 \parallel (\mathbf{u}_2 - \mathbf{u}_1) - g\mu \frac{\mathbf{u}_2}{\parallel \mathbf{u}_2 \parallel}, \tag{3}$$

where $b(x, y)$ defines the topography and gravity acceleration g is reduced by a factor:

$$\kappa = 1 - \rho_1/\rho_2 \tag{4}$$

with ρ_1 the density of water, ρ_2 the density of the granular material and $r = \rho_1/\rho_2$. The first line of $S_{f,1}$ and $S_{f,2}$ represent an empirical friction term between the water and granular layer involving the square of their relative velocity and a drag coefficient m_f. When the water is directly in contact with the bottom—second line of eq. (2), a similar friction between the water and the bottom is assumed involving the Manning coefficient n. These friction terms are used in HySEA and other landside-tsunami models and the detailed study of these friction terms is beyond the scope of this paper. The 3 first equations of system (1) represent the mass, horizontal and vertical momentum balance equations for the water while the forth equation is related to the water incompressibility condition. The two last equations of system (1) represent the mass and horizontal momentum balance equations for the granular layer for which the pressure is assumed to be hydrostatic and a Coulomb-type friction law is used with a the friction coefficient μ (see Section 2.3). In system (1), ∇ is the gradient vector in the horizontal (x, y) plane.

When hydrostatic pressure is assumed for the water layer, eq. (1) are reduced to:

$$\partial_t h_1 + \nabla \cdot (h_1 \mathbf{u}_1) = 0,$$

$$\partial_t \mathbf{u}_1 + \mathbf{u}_1 \cdot \nabla \mathbf{u}_1 + \nabla (g(b + h_1 + h_2)) = S_{f,1},$$

$$\partial_t h_2 + \nabla \cdot (h_2 \mathbf{u}_2) = 0,$$

$$\partial_t \mathbf{u}_2 + \mathbf{u}_2 \cdot \nabla \mathbf{u}_2 + \nabla (g(b + h_2 + (1 - \kappa)h_1)) = S_{f,2}. \tag{5}$$

The non-hydrostatic and hydrostatic versions of HySEA will be used and compared in the following sections for laboratory and field-scale simulations.

It is well known that hydrostatic models (i.e. shallow-water) predict an accurate phase velocity only for values of $kH \ll 1$, where H is the water depth and $k = \frac{2\pi}{\lambda}$ is the wavenumber [in practice when $\frac{H}{\lambda} < 0.05$ (Le Méhauté 1976), i.e. for $kH < 0.1\pi$]. Macias *et al.* (2021a) showed that the HySEA multilayer non-hydrostatic model makes it possible to extend the validity range of the phase velocity but, for one-layer models (i.e. depth-averaged), the dispersive relation deviates from full potential theory for $kH > 2.5$ (see their table 1). In particular, for small landslides occurring far from the shore and at great depth, it is difficult to accurately simulate the first waves emerging on the top of the landslide. However, waves calculated far from this non-valid region are still accurate. Multilayer models strongly improve these results but are out of the scope of this paper.

Let us now continue to simplify the model to show how it can be reduced to the extended version of the SHALTOP model (Section 2.2) that will be used to quantify the error related to topography effects in HySEA. If we assume that the wavelength of the free surface perturbations surface are long compared to the water depth:

$$\nabla (b + h_1 + h_2) = 0, \tag{6}$$

the velocity equation for the granular layer can be simplified using $\nabla h_1 = -\nabla (b + h_2)$. We then obtain the reduced system:

$$\partial_t h_1 + \nabla \cdot (h_1 \mathbf{u}_1) = 0,$$

$$\partial_t \mathbf{u}_1 + \mathbf{u}_1 \cdot \nabla \mathbf{u}_1 + \nabla (g(b + h_1 + h_2)) = S_{f,1},$$

$$\partial_t h_2 + \nabla \cdot (h_2 \mathbf{u}_2) = 0, \tag{7}$$

$$\partial_t \mathbf{u}_2 + \mathbf{u}_2 \cdot \nabla \mathbf{u}_2 + \nabla (g\kappa (b + h_2)) = S_{f,2}.$$

Finally, if we neglect shear friction between the water and the granular layer ($S_{f,1}$ and $S_{f,2}$), the evolution of the granular layer is decoupled from the evolution of the fluid layer. Therefore, the evolution of the granular layer can be obtained from the solution of the system:

$$\partial_t h_2 + \nabla \cdot (h_2 \mathbf{u}_2) = 0,$$

$$\partial_t \mathbf{u}_2 + \mathbf{u}_2 \cdot \nabla \mathbf{u}_2 + \nabla (\kappa g (b + h_2)) = -\kappa g \mu \left(\frac{\mathbf{u}_2}{||\mathbf{u}_2||} \right). \tag{8}$$

This corresponds to eqs (13) and (14) implemented in SHALTOP (Section 2.2) when substituting κg for g, h_2 for h and $\mathbf{u}_2$ for $\mathbf{u}$ with the simplifications $c = 1, s = 0, H = 0$ in SHALTOP (see next section). When the friction between the water layer and the avalanche is neglected, then, the only effect the water plays is a role in the acceleration terms—divide eq. (8) by κ.

2.2 The SHALTOP numerical model

The code SHALTOP solves the depth-averaged equations for dry granular flows on a complex 2-D topography $b(x, y)$ (Bouchut *et al.* 2003; Bouchut & Westdickenberg 2004; Mangeney-Castelnau *et al.* 2005; Mangeney *et al.* 2007a). Contrary to HySEA, the granular flow is assumed to be thin in the direction normal to the topography compared to its downslope extension. The equations are depth-averaged along this normal direction. SHALTOP has been shown to reproduce experimental and natural granular flows, with the limitations inherent to the thin-layer approximation (e.g. Favreau *et al.* 2010; Moretti *et al.* 2012; Peruzzetto *et al.* 2019).

Peruzzetto *et al.* (2021) showed that curvature effects due to a complex topography can drastically change the dynamics and deposit of natural granular flows. They are taken into account in SHALTOP through the curvature tensor of the topography $b(x, y)$:

$$H = \begin{pmatrix} \frac{\partial^2 b}{\partial x^2} & \frac{\partial^2 b}{\partial x \partial y} \\ \frac{\partial^2 b}{\partial x \partial y} & \frac{\partial^2 b}{\partial y^2} \end{pmatrix}. \tag{9}$$

The normal to the topography at each point is calculated through a 3-D unit upward normal vector [we added an arrow on vectors that are not in the (x, y) plane]:

$$\vec{\mathbf{K}} = \left(\frac{-\nabla b}{\sqrt{1 + ||\nabla b||^2}}, \frac{1}{\sqrt{1 + ||\nabla b||^2}} \right) = (-\mathbf{s}, c), \tag{10}$$

where the scalar $c = \cos(\theta)$ is the cosine of the angle between the vertical direction and the normal $\vec{\mathbf{K}}$. The flow is described by:

$$h \geq 0, \mathbf{u}, \tag{11}$$

where h is the thickness of the avalanche in the direction normal to the topography, $\mathbf{u} = (u_d, u_t)$ ($._d$ for downslope and $._t$ for transverse) is a parametrization of the velocity defined in order to simplify the equations with topography, and u is the velocity norm (see Mangeney-Castelnau *et al.* 2005, for more details). In the horizontal Cartesian coordinate formulation, the mass and momentum balance equations model can be expressed as:

$$\partial_t (h/c) + \nabla \cdot (h\mathbf{u}) = 0 \tag{13}$$

$$\partial_t \mathbf{u} + c u. \nabla \mathbf{u} + \frac{1}{c} \left(\mathrm{Id} - \mathbf{s} \mathbf{s}^t \right) \nabla (g (hc + b)) = \frac{-1}{c} \left(\mathbf{u}^t H \mathbf{u} \right) \mathbf{s} + \frac{1}{c} \left(\mathbf{s}^t H \mathbf{u} \right) \mathbf{u} - \frac{g \mu c \mathbf{u}}{\sqrt{c^2 \parallel \mathbf{u} \parallel^2 + (\mathbf{s} \cdot \mathbf{u})^2)}} \left(1 + \frac{\mathbf{u}^t H \mathbf{u}}{gc} \right)_+, \tag{14}$$

where h is the granular thickness in the direction normal to the topography. The subscript $+$ stands for the positive part, $x_+ = \max(0, x)$—see Bouchut and Westdickenberg (2004) and Mangeney-Castelnau *et al.* (2005) for more details. The signature of the thin-layer approximation related to the topography can be observed in the presence of c and $\mathbf{s}$ in the equations, and, in the right-hand side of eq. (14), in the first two curvature terms and in the last term representing the Coulomb-type friction law.

SHALTOP has been designed to simulate dry granular flows. However, through the use of reduced gravity, we model buoyancy even if viscous drag effects are not included. Then, replacing gravity g by κg makes it possible to obtain the submarine flow equations when the drag friction that couples the avalanche and the water column is neglected [see eq. (8) of the simplified HySEA equations in Section 2.1]. Note that in SHALTOP, κ is taken to be equal to eq. (4) for the immersed and dry flow entering water cases, even though in the last case it should have been equal to 1 before the material enters water. This leads to a slower velocity of the aerial part of the collapse for the dry flow entering water case.

2.3 Friction law

In their seminal work, Savage & Hutter (1989) used a Mohr–Coulomb internal rheology with a constant Coulomb basal friction coefficient μ. However, this simple law does not allow reproduction of the steady uniform flows observed in the laboratory for a given range of slope angles. Based on these experiments involving spherical glass beads flowing on a rough bed, Pouliquen (1999) showed that:

$$Fr = \frac{u}{\sqrt{gh \cos(\theta)}} = \beta \frac{h}{h_{\mathrm{stop}}(\theta)}, \tag{15}$$

where u and h are the mean velocity and thickness of the flow, Fr is the granular flow Froude number, $h_{\text{stop}}(\theta)$ is the thickness of the deposit left after a steady uniform flow on a slope inclined at an angle θ and the $\beta = 0.136$ is a constant for glass beads. This observation was used by Pouliquen (1999) to propose an empirical friction law valid for steady uniform flows, with a friction coefficient depending on the thickness and velocity of the flow. Pouliquen & Forterre (2002) extended this law based on experimental measurement of the thickness $h_{\text{stop}}(\theta)$ and of the angle $\theta_{\text{start}}(h)$ at which a layer of thickness h starts to flow. This law was assumed to be valid for the whole range of possible thicknesses and Froude numbers even though the experimental data only concerned steady and uniform flows. The friction law involves three friction angles δ_1, δ_2 and δ_3, the constant β and a fitting parameter L that is of the same order of magnitude as the grain diameter. The angle δ_3 corresponds to the asymptote of the curve $\theta_{\text{start}}(h)$. Depending on the value of the Froude number, the flow is assumed to be in a dynamic ($Fr > \beta$), intermediate ($0 < Fr < \beta$) or static regime ($Fr = 0$) and the friction coefficient can be written as:

$$\mu(h, Fr) = \begin{cases} \mu_1 + \dfrac{\mu_2 - \mu_1}{1 + \frac{h\beta}{LFr}}, & Fr \geq \beta, \\ \left(\dfrac{Fr}{\beta}\right)^{\xi}\left(\mu_1 + \dfrac{\mu_2 - \mu_1}{1 + \frac{h}{L}} - \mu_3 - \dfrac{\mu_2 - \mu_1}{1 + \frac{h}{L}}\right) + \mu_3 + \dfrac{\mu_2 - \mu_1}{1 + \frac{h}{L}}, & 0 < Fr < \beta, \\ min\left(\mu_3 + \dfrac{\mu_2 - \mu_1}{1 + \frac{h}{L}}, |\tan\theta i - \nabla h|\right), & Fr = 0, \end{cases} \tag{16}$$

where $\mu_1 = \tan\delta_1$, $\mu_2 = \tan\delta_2$, $\mu_3 = \tan\delta_3$, $\mathbf{i}$ is the unit vector in the x-direction and L is the typical grain diameter. Note that the friction law in the intermediate regime is given by a power law extrapolation between the friction laws in the static and dynamic friction regimes. Simulation results have been shown to be poorly affected by the value of the empirical parameter ξ as soon as $\xi < 10^{-2}$ (Pouliquen & Forterre 2002; Mangeney *et al.* 2007a). As in these studies, we choose $\xi = 10^{-3}$. Several studies have focused on these friction laws and possible extensions to reproduce laboratory experiments on erosion/deposition waves (Mangeney *et al.* 2007b; Edwards & Gray 2014; Edwards *et al.* 2017, 2019; Russell *et al.* 2019) or self-channelling flows and levee formation (Mangeney *et al.* 2007a; Rocha *et al.* 2019) but the behaviour of granular material in the intermediate regime is still largely unknown. This $\mu(I)$ type rheology has been first derived from dry granular flows and further extended to account for grain-fluid effects by changing the inertial number or even by introducing dilatancy (e.g. Pailha & Pouliquen 2009). Introducing these grain fluid effects is beyond the scope of this paper.

In this study, we use the Pouliquen & Forterre (2002) friction law in HySEA and SHALTOP to simulate subaerial, immersed and dry entering water granular flows observed at the laboratory scale (Section 4) and field scale (Section 5).

3 EXPERIMENTAL DATA

Landslide-generated tsunamis have been benchmarked. At the laboratory scale, benchmarking mainly focused on comparison between simulated and recorded water waves on gauges (Kirby *et al.* 2022). Indeed, experimental data rarely provide both the detailed time evolution of the granular mass and the water waves. For example, only pictures of some granular flows are provided in the NTHMP Landslide Tsunami Benchmarking Workshop (Kirby *et al.* 2022) even though laboratory experiments on water waves generated by granular flows are more and more common (e.g. granular column collapses on a horizontal bed by Robbe-Saule *et al.* 2021, Sarlin *et al.* 2021 or gas-fluidized granular collapse by Bouguoin *et al.* 2020, 2021). Furthermore, benchmark exercises involve a few experiments in different settings and allow the fitting of model parameters to reproduce the water waves. The fitted parameters are found to be different for each experiment, with values that are not always physically meaningful, such as for example the low friction coefficients used by Macias *et al.* (2021b) in the Pouliquen and Forterre friction law.

To quantify the error in HySEA simulations of granular flows with independently measured friction coefficients (i.e. without calibration), we process a series of laboratory experiments on granular masses released on sloping to horizontal beds performed by Viroulet *et al.* (2014, 2019) for water gauges in entering water and dry experiments; unpublished data for immersed experiments and analysis of dynamics for all three configurations). These new experiments provide a unique data set of water waves generated by granular flows together with the time change of the granular mass profiles, conducted in the same experimental set-up for different slope angles, initial conditions (subaerial, immersed and dry flow entering water) and grain diameters.

These experiments represent demanding conditions for the models because (i) the shallow-water approximation is not always satisfied for the granular mass (especially at the beginning), (ii) the wave generation area has characteristics out of the range of validity of the dispersive model and (iii) the bottom slope is far from horizontal and therefore the horizontal/vertical reference frame is not appropriate to describe the granular flow. As a result, the error in HySEA results when simulating these experiments can be considered in the upper range, making it possible to clearly highlight the limits of such models. Quantification of this error is essential for analysing the results obtained when applying the model to simulate field-scale landslides and tsunamis where characteristic dimensions can be, at some locations and/or times, outside of the limits of model assumptions.

3.1 Experimental setup

The experimental set up consisted of a 2.20 m long, 0.20 m wide and 0.40 m high wave tank with a reservoir filled with 2 kg of glass beads of diameter $d = 4$ mm and density $\rho = 2500$ kg m^{-3} that is initially released on the slope (Fig. 1); the set-up is similar to the one described in Viroulet *et al.* (2014) where details can be found.
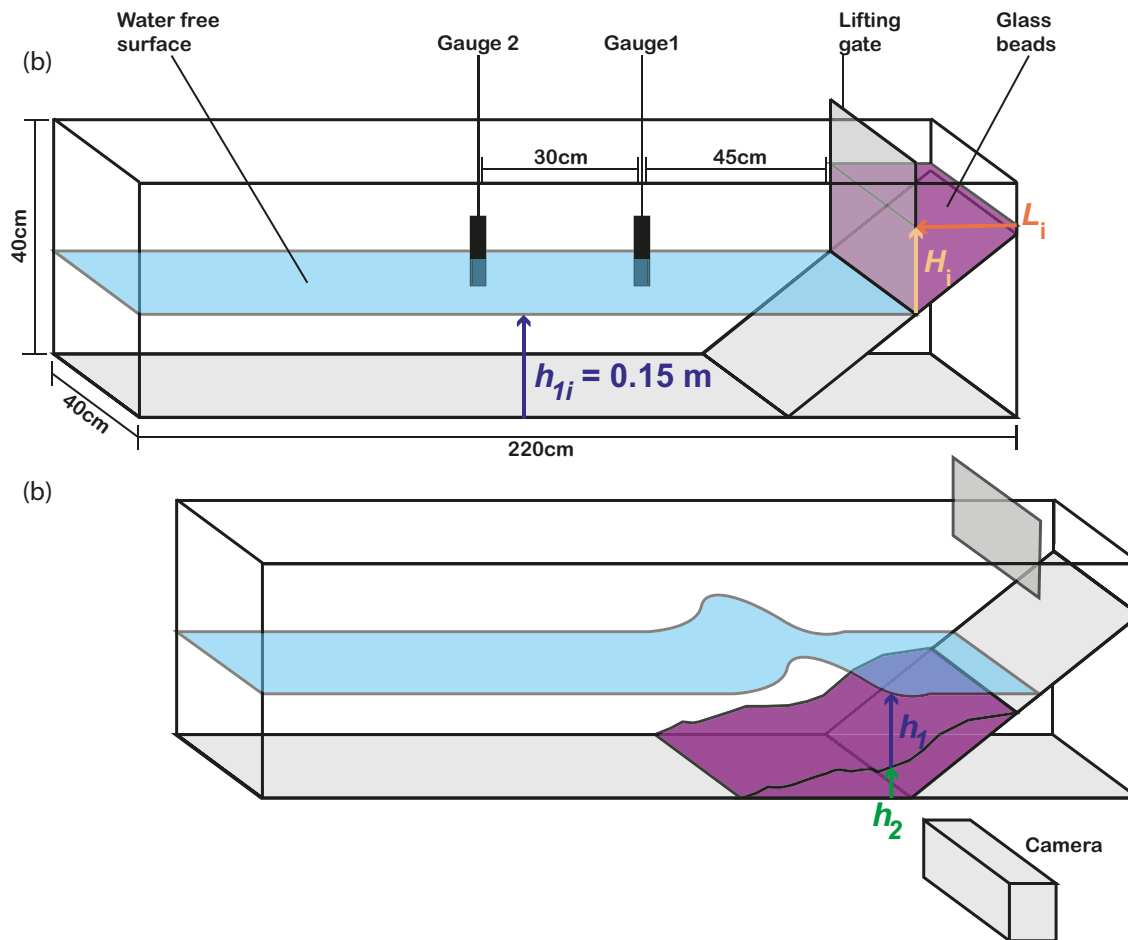
Figure 1. Experimental set-up: (a) initial set-up with relative position of the gauges (1, 2 and 3) and initial mass. (b) During the experiment showing the thickness of both the granular layer and water column and the position of the camera.

Several experiments were performed with different slope angles. For each slope angle, depending on the initial water depth, the granular collapse was either dry, fully immersed or dry entering water (Fig. 2). A layer of the same material as the collapsing beads was glued on the slope and on the bottom of the tank. A vertical gate was used to maintain the initial granular materials of maximum thickness $H_i = 0.15$ m from the surface of the beads glued on the bottom of the tank (Fig. 1). This gate was opened vertically using a system of mass and pulley. The velocity of the gate removal was 1.2 m s^{-1}, lasting about 0.11 s for a granular flow duration of 1.3–2.2 s. In this study, we focus on experiments obtained on two slope angles (35° and 45°) with three initial water heights above the surface of the particles glued on the bottom of the tank (0, 0.15 and 0.30 m). An additional experiment was studied for the dry case with $d = 1.5$ mm. The evolution of the granular collapses and the generated waves was recorded using a high-speed camera at a hundred frames per second and we extracted their profiles by image processing every 0.1 s. The error related to the manual picking (each measurement is repeated three times), image distortion, set-up, etc. is estimated to be about $1.5d \approx 6$ mm for $d = 4$ mm. The time evolution of the water free surface during the propagation was also recorded by several wave gauges. Table 1 summarizes the main characteristics of these experiments.

3.2 Granular flow

The dynamics and deposit as well as the generated water waves obviously depend on the configuration (dry, immersed or dry flow entering water) as observed for example on the 35° slope angle (Figs 2 and 3a–c). Note that the gate affects the shape of the released mass that is entrained by the gate during the initial instants when it is opened (Fig. 3) as was also observed in granular collapse experiments on inclined planes (see e.g. figs 6a and c of Mangeney *et al.* 2010).

In the dry case, the granular mass reaches the bottom of the tank about 0.4 s after the release (Fig. 2c). The granular flow is relatively thin on the slope (2–3 cm). After reaching the bottom, the flow slows down (Fig. 2c) and stops at about 40 cm from the gate (Figs 2d and 3a).

In the immersed case (Fig. 2e), the flow is slower and thicker (around 5 cm) because of strong interactions with water (Figs 2f–g) and reaches the slope break 0.6 s after the opening of the gate. While flowing down the slope, the flow front becomes thicker than the rest of the flow (Fig. 2g) because of dilatation effects (Section 3.3). The front deposit is located 5 cm further than in the dry case (Figs 2h and 3b). The time-series of the granular profiles (Fig. 3) show that the flow is faster on the slope in dry conditions than in the immersed case because of
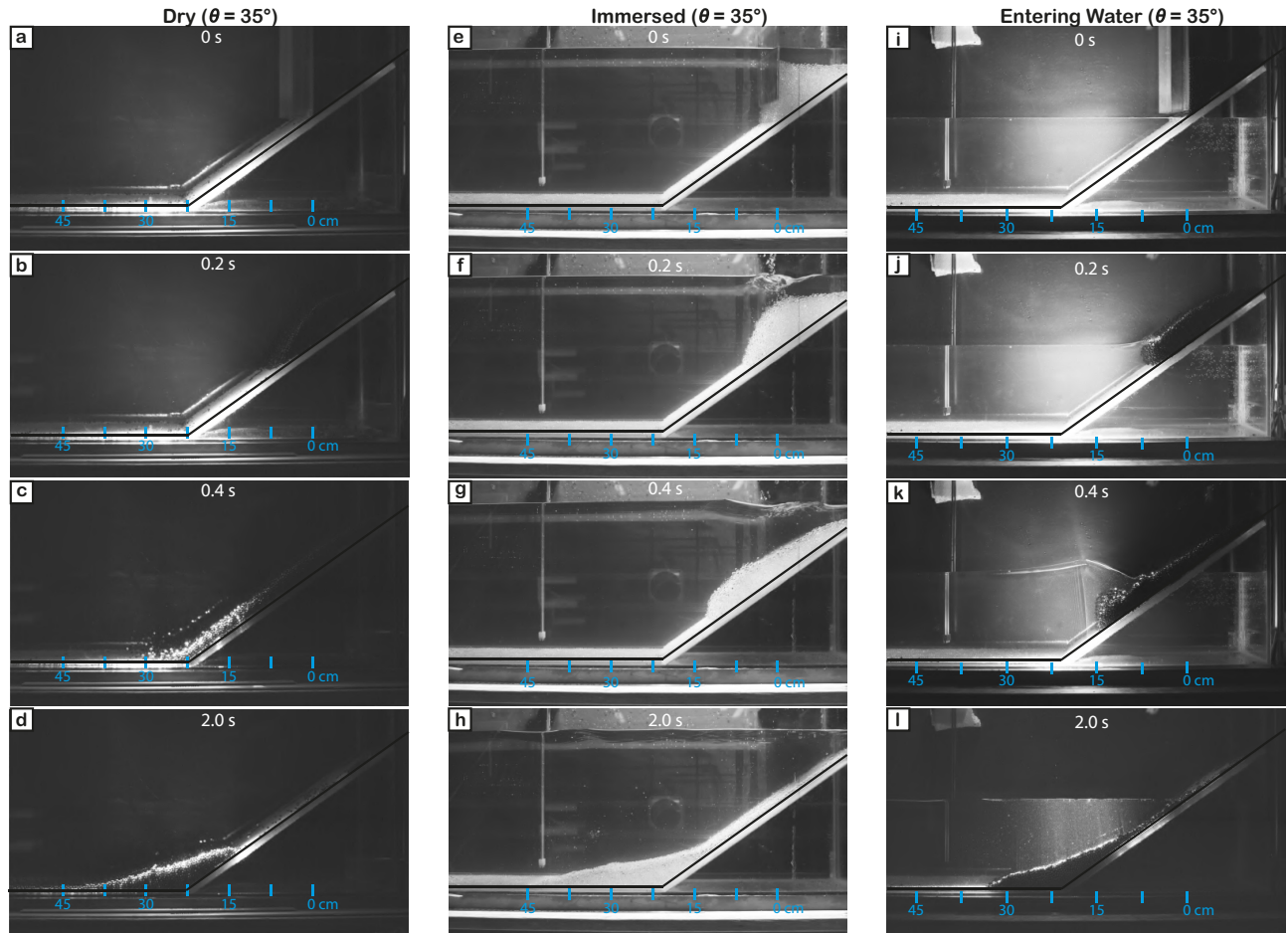
Figure 2. Snapshots of three different experiments (Table 1) showing the time evolution of the granular collapse in dry (a–d) (Experiment 1 in Table 1), immersed (e–h) (Experiment 2 in Table 1) and dry flow entering water (i–l) (Experiment 3 in Table 1) configurations. The experiments are performed on a bed with a constant slope $\theta = 35°$ followed by a horizontal plane.

reduced gravity for underwater flow, whereas the deposits extend further in the immersed condition because of less deceleration at the end of the flow. This may be due to the strong contraction of the granular mass (see Section 3.3) in the immersed case as it reaches the flat bottom, inducing an increase in pore pressure, thus reducing the granular friction force (e.g. Rondon *et al*. 2011; Pailha & Pouliquen 2009; Bouchut *et al*. 2016b, 2017). The deposit shapes are also different with more mass located near the front in the immersed case.

Finally, for the case of the dry flow entering water (Fig. 2i), the front is strongly decelerated and rounder as the mass enters the water (Fig. 2j) but it then accelerates sufficiently to become similar to the fully immersed case (Fig. 3). The flow velocity is still however lower than in the dry case. During its propagation down the slope, the granular front is thick (3–5 cm) and the flow surface has a complex shape (Fig. 2k). When the flow reaches the bottom, the flow decelerates more rapidly than in the immersed case, leaving a significant part of the deposit upslope (Fig. 2l). This larger deceleration in the dry mass entering water case may be due to the smaller dilatation of the flow during its spreading (Section 3.2.2) leading to subsequent smaller compaction, inducing a smaller increase in pore fluid pressure and thus a higher friction force on the grains (Bouchut *et al*. 2016a,b). The shorter run-out distance (i.e. front position of the deposit) of the dry mass entering water case compared to the dry case may be due to the friction with water, especially when the mass enters it.

For a 45° slope angle, the overall behaviour is similar to the 35° experiments (Figs A1 and 3d–f). As the slope angle increases, the surface of the granular mass becomes more irregular (Figs A1g, k compared to Figs 2g, k). At 45°, the flow down the slope is faster for the case of a mass entering water than for the fully immersed case, both still slower than for the dry case (Fig. A2). On the 45° slope, the travelling distance on the horizontal plane is slightly smaller than at 35°, despite higher inertial effects, and less material remains on the slope. This decrease in run-out for 45° compared to 35° could be related to the longer sloping part that compensates for the higher gravitational force and higher pressure gradients related to a higher initial height H_i at 45° (Fig. A2). The variation of the slope angle (within this range) does not greatly affect the run-out distance since the abrupt change of the topography towards the horizontal plane greatly slows the flow and is the main effect controlling the mass stopping. As for the 35° slope, the run-out distance is the largest in the immersed case, then in the dry case, while the shortest run-out is observed in the dry mass entering water case.

Table 1. Summary of the experimental results and their numerical simulations with θ the slope angle and h_{1i} the initial water height (in cm), H_i and L_i the height and length of the initial mass (in cm), and the friction angles used to perform the simulations. Friction angles and run-out distance obtained with HySEA fitted on SHALTOP are written in brackets. We used the following parameters: Experiments 1–6 used 4 mm beads, experiments 7 and 8 used 1.5 mm beads. For experiments 1, 4, 7, 8 the water level is 0. For experiments 2, 5, the water level is 30 cm. For experiments 3, 6, the water level is 15 cm. For experiments 1-3 and 7 the slope angle is 35°, for experiment 4– and 8 the slope angle is 45°. For experiments 1–6 the non-fitted friction angles ($\delta_1, \delta_2, \delta_3$) used in the simulations are $\delta_1 = 22.1°$, $\delta_2 = 31.8°$, $\delta_3 = 23.3°$. For experiment 7 and 8 the non-fitted friction angles ($\delta_1, \delta_2, \delta_3$) used in the simulations are $\delta_1 = 24.5°$, $\delta_2 = 34.2°$, $\delta_3 = 25.7°$. Fitted angles used in HySEA simulation of experiment 1–3 are $\delta_1 = 27.1°$, $\delta_2 = 36.8°$, $\delta_3 = 28.3°$, in experiment 4-6 the fitted angles are $\delta_1 = 29.1°$, $\delta_2 = 38.8°$, $\delta_3 = 30.3°$. Fitted angles used in HySEA simulation of experiment 7 are $\delta_1 = 29.5°$, $\delta_2 = 39.2°$, $\delta_3 = 30.7°$, and $\delta_1 = 31.5°$, $\delta_2 = 41.2°$, $\delta_3 = 32.7°$ for simulation of experiment 8.

		Initial mass height H_i, length L_i (cm)	Run-out distance from the gate (cm)	Difference of the run-out distance between experiment and simulations (cm)	Time-shift for gauges Δt (s)	Maximum amplitudes of the generated waves at Gauge 1 (cm)	
						Hydrostatic	Non hydrostatic
Experiment 1 (35° Dry)	Experiment	$H_i = 10.3$ $L_i = 13.1$	39.25	-	-		-
	HySEA Non-fitted (fitted)		52.32 (43.36)	13.07 (4.11)	-	-	-
	SHALTOP		39.68	0.43	-	-	
Experiment 2 (35° Immersed)	Experiment	$H_i = 11.0$ $L_i = 13.2$	44.94	-	-	0.32 / –0.65	
	HySEA Non-fitted (fitted)		52.96 (43.68)	8.02 (1.26)	0.15	0.7 / –0.25	0.59 / –0.57
	SHALTOP		37.44	7.5	-		-
Experiment 3 (35° Entering Water)	Experiment	$H_i = 10$ $L_i = 13.53$	34.7	-	-	1.53 / –1	
	HySEA Non-fitted (fitted)		80 (62.7)	45.3 (28)	0.385	2.88 / –0.08	1.32 / –0.3
	SHALTOP		37.4	2.7	-	-	
Experiment 4 (45° Dry)	Experiment	$H_i = 11.4$ $L_i = 10.78$	38.6	-	-		-
	HySEA Non-fitted (fitted)		56.8 (43.36)	18.2 (4.76)	-	-	-
	SHALTOP		37.1	1.5	-	-	
Experiment 5 (45° Immersed)	Experiment	$H_i = 11.5$ $L_i = 10.94$	41.84	-	-	0.65 / –0.88	
	HySEA Non-fitted (fitted)		57.76 (44.0)	15.92 (2.16)	0.18	0.95 / –0.34	0.59 / –0.87
	SHALTOP		37.12	4.72	-	-	
Experiment 6 (45° Entering Water)	Experiment	$H_i = 12.0$ $L_i = 10.88$	33.78	-	-	2.1 / –1.4	
	HySEA Non-fitted (fitted)		92.64 (72.32)	58.86 (38.54)	0.37	3.37 / –0.32	1.49 / –0.46
	SHALTOP		37.12	3.34	-	-	
Experiment 7 (35° Dry)	Experiment	$H_i = 10.32$ $L_i = 14.1$	38.56	-	-		-
	HySEA Non-fitted (fitted)		48.32 (39.84)	9.76 (1.28)	-	-	-
	SHALTOP		35.84	2.72	-	-	
Experiment 8 (45° Dry)	Experiment	$H_i = 11.8$ $L_i = 11.7$	39.84	-	-		-
	HySEA Non-fitted (fitted)		52.48 (40.16)	12.64 (0.32)	-	-	-
	SHALTOP		36.0	3.84	-	-	

3.3 Dilatation of the granular material

Even though most of the numerical models assume that the granular layer is incompressible, it is well known that granular flows experience both dilatation and compaction (e.g. Roux & Radjai 1997; Rondon *et al*. 2011; Pailha & Pouliquen 2009; Bouchut *et al*. 2016a,b, 2021). This compressibility impacts the shape and velocity of the flow and thus may be a source of error when not accounted for in numerical models, especially for granular flows under water (Rondon *et al*. 2011; Bouchut *et al*. 2021; Rauter 2021). We quantify these effects here to better interpret the comparison between incompressible codes and experimental results and therefore discriminate the origins of the error.

Dilatation and compaction of the whole mass are estimated here by measuring, on the snapshots of the experiments, the evolution of the area of the longitudinal profile of the flowing and deposited mass A with respect to the area of the profile of the initial mass (before collapse) A_i. At each time, we calculate the relative difference $(A–A_i)/A_i$. Fig. 4 shows the time evolution of the dilatation/compaction of the mass for
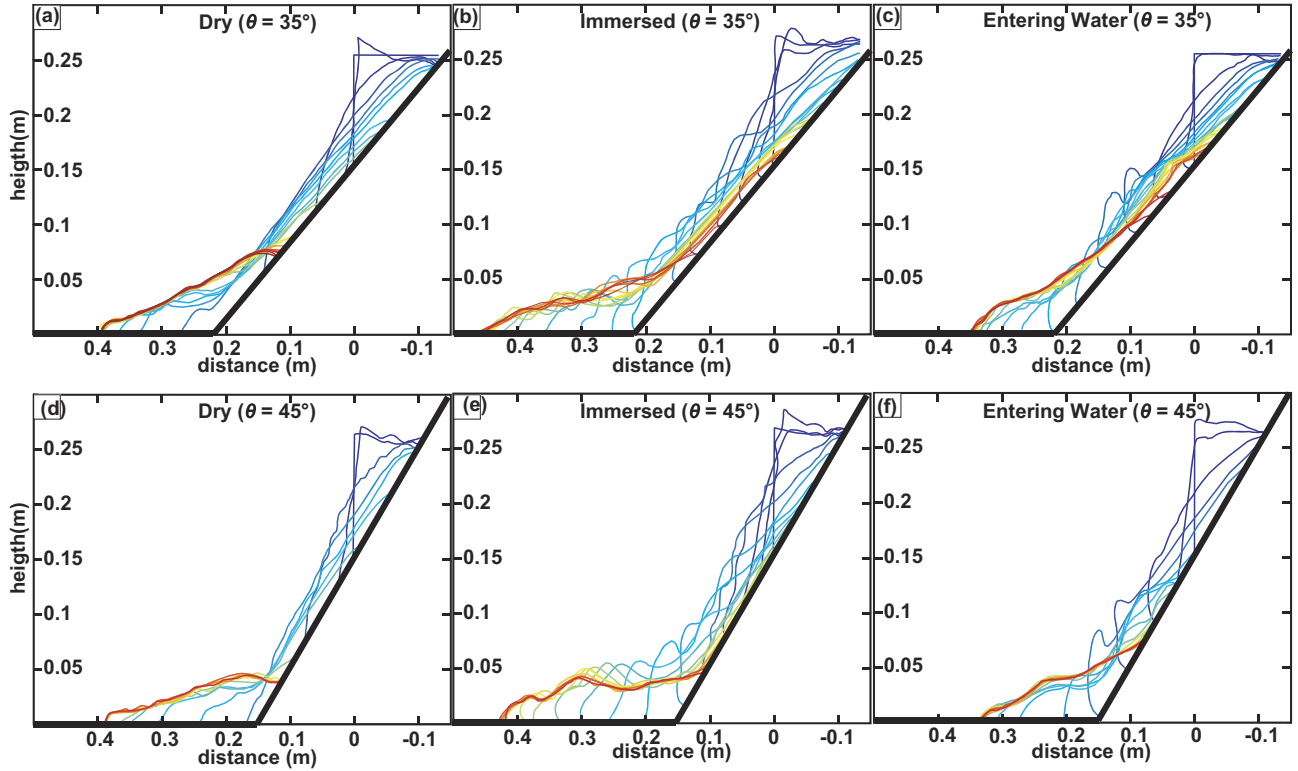
Figure 3. Position of the hand-picked (i.e. visual inspection without image processing) avalanche surface for the six experiments (Table 1) in dry (a, d), immersed (b, e) and dry flow entering water (c, f) configurations with slopes $\theta = 35°$ (a–c) and $\theta = 45°$ (d–f). The surface positions are represented every 0.1s.
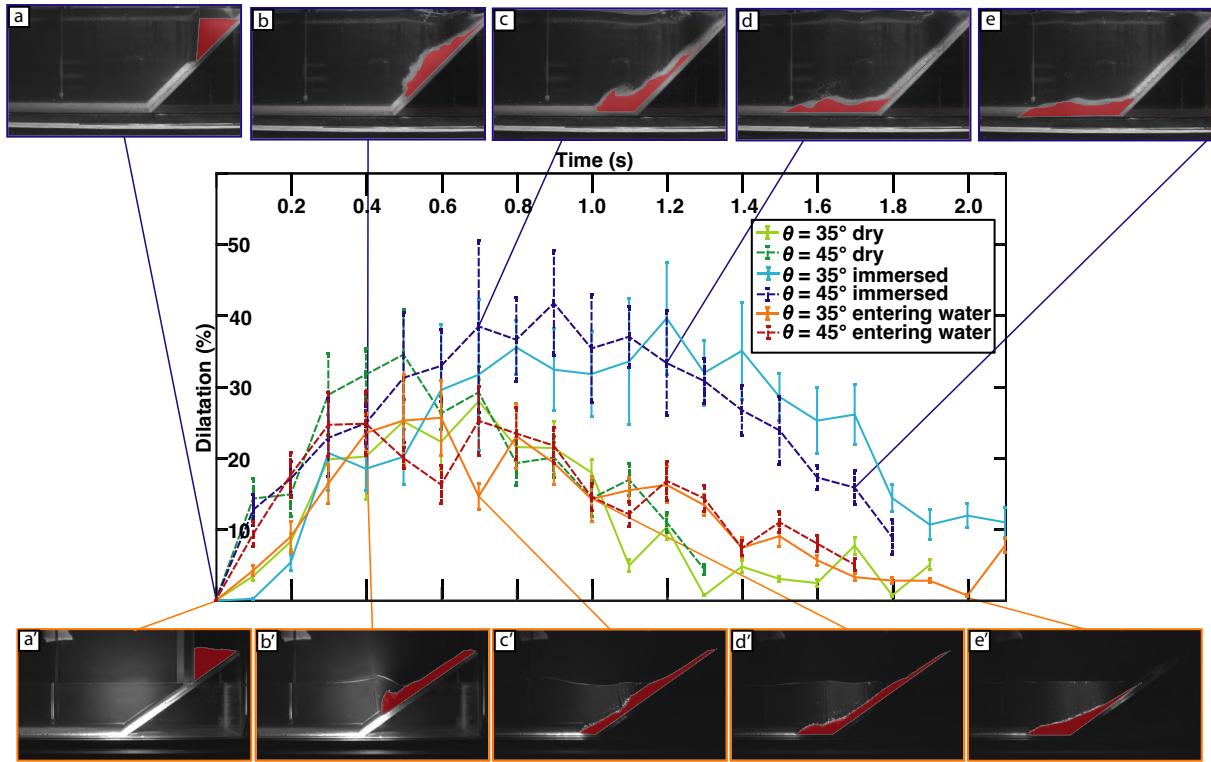

Figure 4. Evolution of the material dilatation during the different experiments. Error bars represent the variability of the measurement of the landslide-surface. (a–e): Immersed collapse on a 45° slope angle. (a'–e'): Dry flow entering water collapse on a 35° slope. The red surface represents the measured area of the longitudinal profile of the material.

the different initial configurations and slope angles. The error bars represent the variability of the measurement of these areas on the different recorded images.

The two dry experiments reach a maximum dilatation of about 27 per cent at 35° and 35 per cent at 45°, respectively. Sometimes after reaching the bottom of the tank, the mass compacts, leading to a deposit with nearly the same volume as the initial released mass. These results agree with the experimental measurements shown in Martin *et al.* (2017, their fig. 6) where a maximum dilatation of 10 per cent was observed for dry granular column collapse on a 22° slope within a 0.2 m wide channel. As expected, the maximum dilatation for the two immersed experiments is much higher than for the dry experiments, reaching about 38 and 42 per cent for the 35° and 45° slope angles, respectively. As in the dry case, the maximum dilatation is reached earlier on the 45° slope than on the 35° slope. The deposits are relatively compact (a maximum of 10 per cent dilatation compared to the initial released mass). For the dry granular collapse entering water, the material dilates as in the dry configuration and compacts, probably due to the impact with water. Then the flow dilates again with a maximum dilatation much lower than in the fully immersed case, reaching a maximum of ∼25 per cent for both slope angles. It finally compacts with a characteristic time slightly longer than in the dry case and recovers its initial compaction.

3.4 Observed water wave

During the collapse in the immersed case, a wave is generated at the free surface (Figs 2f–g and A3) that is impacted by the mass released upon removal of the immersed gate. In the dry flow entering water case, waves are generated at the impact with amplitudes much higher than for the immersed configuration (Figs 2j and k). In both 35° and 45° slope configuration, for the dry flow entering water case, the maximum is reached by the first wave (Figs A4 and A5).

4 SIMULATION OF LABORATORY EXPERIMENTS

4.1 Simulation of granular flows

Numerical simulations have been performed with the HySEA and SHALTOP codes using the friction law of Pouliquen & Forterre (2002; eq. 16). To allow calculating curvature terms and avoid numerical instabilities, we used a polynomial of degree 2 to smooth the transition between the sloping and horizontal plane (Fig. 5). The first simulations were obtained by simply adapting the rheological parameters measured by Pouliquen & Forterre (2002) to our 0.5 mm glass beads, in order to assess the model performance without any fitting procedure. In their experiments, they took $L = 0.65$ mm corresponding to $1.3d$. Here we thus take $L = 5.2$ mm for $d = 4$ mm and $L = 1.95$ mm for $d = 1.5$ mm. In experiments with the same set-up, Viroulet *et al.* (2014) only measured the avalanche angle δ_3. To calculate δ_1 and δ_2, we impose the same difference between the friction angles as in Pouliquen & Forterre (2002) $\delta_3 - \delta_1 = 1.2°$ and $\delta_2 - \delta_1 = 9.7°$. We thus take $\mu_1 = 0.406$ ($\delta_1 = 22.1°$), $\mu_2 = 0.620$ ($\delta_2 = 31.8°$), $\mu_3 = 0.430$ ($\delta_3 = 23.3°$) for $d = 4$ mm and $\mu_1 = 0.456$ ($\delta_1 = 24.5°$), $\mu_2 = 0.680$ ($\delta_2 = 34.2°$), $\mu_3 = 0.481$ ($\delta_3 = 25.7°$) for $d = 1.5$ mm (see Table 1). Note that the uncertainty of the avalanche angles is about 1° in Viroulet *et al.* (2014). We also set $\beta = 0.136$ as in Pouliquen & Forterre (2002).

One of the objectives of comparing HySEA and SHALTOP (Figs 5 and A6) is to quantify the error in HySEA simulations due to the shallow-water approximation and depth-averaging, both done in the vertical direction, inducing errors in the handling of topography effects. The subsequent step will be to calibrate the friction angle δ_1 in HySEA in order to artificially compensate for these errors (full green lines in Figs 5 and A6). Indeed, as we impose $\delta_3 - \delta_1$, $\delta_2 - \delta_1$, β and L, the only fitting parameter of the friction law is δ_1.

Error quantification from comparison between models and experiments is trickier since the gate opening (Ionescu *et al.* 2015, their figs 14 and 15), wall effects (Martin *et al.* 2017, fig. 4f; Fernandez-Nieto *et al.* 2018, their fig. 12b) and diatancy (Fig. 4; Rondon *et al.* 2011, Bouchut *et al.* 2017, their fig. 2, Bouchut *et al.* 2021) are not taken into account in the models. These processes substantially affect the granular flow and the generated waves, inducing an error expected to be about 15–20 per cent in the front velocity and deposit. Furthermore, there is some uncertainty on the initial shape of the released mass (Figs 2 and 3) because of some lateral heterogeneity of the grain distribution and gate impact. When comparing models with experiments, this error must be kept in mind, as well as the experimental error related to data processing (about 15 per cent).

4.1.1 Comparison between HySEA and SHALTOP to assess topography error

To compare HySEA and SHALTOP, we first set to zero the friction between the water and the granular layer ($m_f = 0$) and the Manning coefficient ($n = 0$) in HySEA [see expressions (2) and (3)]. At a 35° slope angle, for the dry collapse configuration, the material flows rapidly down the slope with HYSEA (green dotted line), significantly faster than with SHALTOP (red solid line). However, both simulations flow faster than the experiments (Fig. 5b). Such overestimation of the flow velocity in shallow-water models is well known but our results show that the error related to the horizontal/vertical reference frame is significant since both models are shallow-water. As a result, the global shape of the mass is more elongated than in the experiments, with a thin layer of material at the front (1 to 2 cm) and a thicker part at the rear, around 4 cm (Fig. 5b). The thickness of the granular layer along the slope in the experiments is greater, partly because of strong dilatation effects at 0.4 s, as detailed in Section 3.3, not taken into account in the models. SHALTOP gives a more accurate representation of the experimental
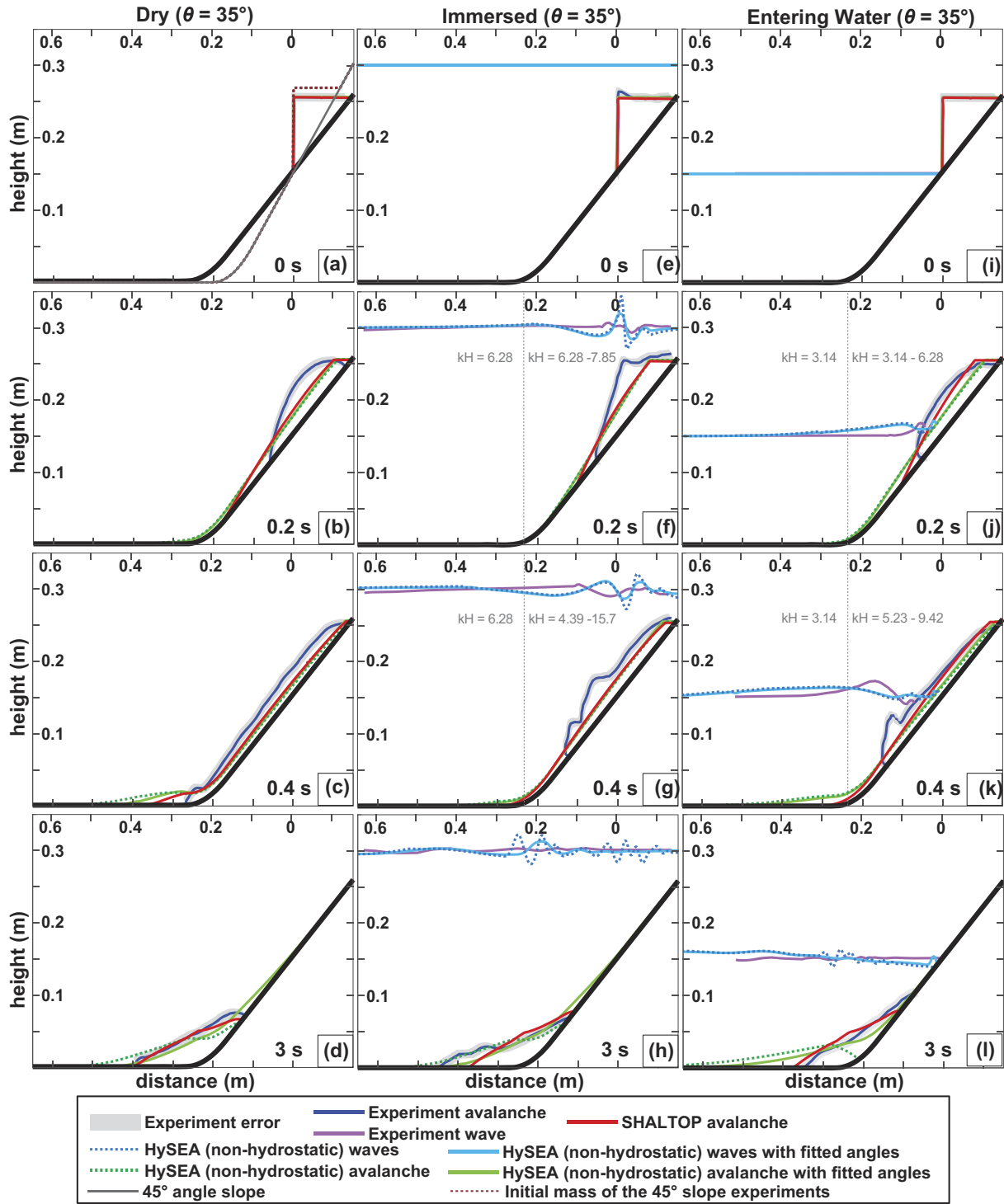
Figure 5. Comparison between experimental and numerical simulations of a granular collapse and potential generated water waves (non-hydrostatic) on a 35°slope in dry (a–d) (Experiment 1 in Table 1), immersed (e–h) (Experiment 2 in Table 1), and dry flow entering water configurations (i–l) (Experiment 3 in Table 1) for beads of 4 mm in diameter. The thick light grey line around the blue line represents experimental error. The bottom topography (grey line) and initial mass (dashed dark red line) of the 45° slope experiment are superimposed on (a) to visualize the difference in the initial and boundary conditions for θ = 35° and θ = 45°. The vertical dotted grey lines on (f, g, j, k) represent the separation between the range of values of *kH* for the generated waves in the area above the sloping bed and that in the area above the horizontal bed.

deposit with a difference in the run-out distance within the range of the experimental error compared to an overestimation of the run-out of about 10 cm with HYSEA (Fig. 5d). The tail of the deposits is also closer to the tail in the experiment. The global shape of the deposit is well reproduced with SHALTOP without any fitting procedure. These differences between HySEA and SHALTOP are partly because of the handling of topography effects as shown in Delgado-Sanchez *et al*. (2020, their fig. 5a).

For the fully immersed case, the granular material in HYSEA also flows faster than in SHALTOP (Figs 5f and g). They both flow faster and are thinner than in the experiment, even though the difference between the simulated and observed front velocity is smaller than in the dry case. As a result, HYSEA generates a water wave a bit earlier than in the experiments. For simulation of the avalanche part, as both models neglect wall, gate and dilatancy effects, the differences between the models should mainly be the result of different handling of topography effects. The run-out distance in the experiment is longer than the distance obtained by SHALTOP, probably because of dilatancy effects (see discussion section 3.3), and shorter than the distance obtained by HySEA (Fig. 5h). SHALTOP reproduces well the emplacement and shape of the tail of the deposit. This is also the case for HySEA, with a higher error. For the initially dry collapse impacting water, the simulated granular flows are also faster and thinner than in the experiment, with a more regular surface (Figs 5j and k). HySEA is again faster than SHALTOP, with greater differences than in the immersed case (compare Figs 5g and k). This could result from the fact that in SHALTOP, $\kappa = 1 - \rho_1/\rho_2$ within the whole mass even though, for the aerial part of the collapse, the value should have been $\kappa = 1$ as detailed in Section 2.2. The overall shape of the deposit obtained with SHALTOP is much closer to the experiment than those from HYSEA (Fig. 5l). The run-out distance in SHALTOP is slightly longer (by 2 cm) than in the experiment (Fig. 5l), while HYSEA overestimates the run-out by more than 20 cm, consequently significantly shifting the global deposit emplacement (Fig. 5l).

Similar results are obtained for the 45° slope angle simulations (Fig. A6). For all configurations, SHALTOP better reproduces the dynamics and deposit. HySEA flows are always faster than those of SHALTOP, leading to overestimation of the position of the deposit and its run-out distance. SHALTOP captures relatively well the deposit shape and run-out distance in all configurations and slopes without fitting the parameters. As a result, topography effects play a crucial role in these extreme configurations and should at least be empirically corrected in HySEA and more generally in all models where the flow is assumed to be shallow in the vertical direction instead of in the slope-perpendicular direction.

4.1.2 HySEA calibration using SHALTOP

To empirically reduce the overestimation of the spreading velocity due to inaccurate handling of topography effects, we quantified the increase in the friction angle required in HySEA to obtain results closer to the granular deposit obtained with SHALTOP. Our objective here was not to make a fine calibration but to provide an idea of the approximate artificial increase of the friction coefficient in HySEA required to compensate for errors in the handling of topography. This will help us better interpret the field-scale simulations in section 5. The calibration strategy used here rely on the fact that HySEA solves the same equations than SHALTOP except for the curvature terms. Another strategy would have been to calibrate HySEA on the recorded water waves as done in Macias *et al*. 2021b, leading to unphysically low friction coefficients for the granular flow, different for each cases, with overestimation of the run-out distance. This could be related to the large number of parameters to fit in the landslide-tsunami model making the fitting non unique and to the approximations made in the wave propagation model, artificially corrected by changing the friction coefficient in the landslide model. Fitting both run-out and water wave data would be more appropriate for accurate wave propagation codes since generated waves encode information on the granular flow dynamics. This is indeed what is done in landslide seismology where it was shown that fitting landslide models on seismic data provide a unique way to get friction parameters relevant to the flow dynamics and not only to the deposit (e.g. Moretti *et al*. 2012, 2015, 2020). This is possible because low frequency wave propagation generated by landslides is well reproduced by Earth Green's function. Another aspect that support using the run-out in our fitting approach is that it is generally the only known field data as in the Martinique case studied here. Obviously, if wave data are available, their use would refine calibration of landslide–tsunami models as it was done with tsunami data in Gylfadottir *et al*. (2017).

The solid green lines in Figs 5 and A6 show the simulations obtained with the values of δ_1 in HySEA fitted to match the SHALTOP results in the 35° dry experiment. Then, we kept this value constant to investigate as to whether it also improves the results in the other configurations at the same slope angle. The friction angle δ_1 has to be increased by 5° in HySEA for a 35° slope angle and by 7° for a 45° slope angle. This fitting little affects the simulation at the initial times (up to 0.2s) as the friction force is small compared to the inertia forces at these instants (Mangeney-Castelnau *et al*. 2003, their fig. 16). However, it improves the results later on by clearly slowing the flow, leading to better estimates of the deposit for all cases, even though the simulated deposit shape is always more elongated, leaving a thin deposit upslope that is neither observed in SHALTOP nor in the experiments. This may be due to the increase of δ_2 that has a dominant impact at low velocities (Mangeney-Castelnau *et al*. 2005, their fig. 15). However, such thin flows on the slope should only have a small impact on generated water waves.

In real case scenarios, the slopes are often gentler for the major part of the landslide path. When fitting HySEA to SHALTOP for similar dry configurations we obtained an increase of 0.5°, 0° and 0° for granular collapses on 20°, 10° and 0° slopes, respectively (Fig. A7).

Finally, the HySEA simulations show that there are almost no differences between the granular flows calculated for hydrostatic and non-hydrostatic descriptions of the water layer (Figs A8 and A9). Note that the equations for the avalanche layer are always hydrostatic in HySEA. More differences would obviously be observed if a non-hydrostatic contribution were added for the granular flow (Garres-Diaz *et al*. 2020; Zhang *et al*. 2021a), but this is outside the scope of this paper.

4.1.3 Influence of grain diameter

We also tested the influence of bead diameter on the experiments and simulation results in the dry case. We took $d = 4$ mm and $d = 1.5$ mm in the experiments and made the corresponding simulation with the L parameter chosen accordingly, $L = 5.2$ mm and $L = 1.95$ mm, respectively. The experiments were performed again on two different slope angles of 35° and 45° (Fig. A10). There are only small differences in the flow and deposit with the two grain diameters. The granular mass made of 4 mm particles flows slightly faster and further than the 1.5 mm particles for the two slope angles. The deposit at the rear of the mass is slightly more rounded and further downslope for the 4 mm particles. Depending on the experiment and time, the differences are slightly higher or within the uncertainty of the experimental measurements. Interestingly the simulations qualitatively reproduce these small differences.

4.2 Simulation of water waves

The simulations and experimental results are compared at two gauges located at 45 and 75 cm from the gate, respectively. The simulations are shifted by a time t because the wave is generated too early in simulations because of the higher flow velocity inherent to shallow-water models (see Table 1 and arrows in the figures for the values of this time-shift). We used the same time-shift for the hydrostatic and non-hydrostatic simulations. The Figs A4 and A5 show that for both the immersed and dry entering water cases, the non-hydrostatic model is needed to well reproduce the observed waves. However, even if the long wavelength waves at the gauges are well reproduced by the simulation (Figs A4, A5 and A11), the water waves just above the granular mass, with shorter wavelengths, are poorly handled. This is partly due to the too high value of kH in this zone (see numbers in grey in Fig. A11), outside of the validity domain of the model (see discussion in Section 2.1). This is a key issue in this kind of models that should be deeper investigated but that is beyond the scope of this paper. Furthermore, complex physical processes occur at the impact of a granular mass with water that are not described in the simple depth-averaged model used here (Bougouin *et al.* 2020).

4.2.1 Influence of water-avalanche, and water-bottom and granular friction

As we wanted to calibrate HySEA using SHALTOP (using the run-out distance) to artificially correct for topography effects, we did not include friction between the granular layer and the water ($m_f = 0$) in the previous sections. We also assumed no friction between the water and the bottom ($n = 0$). These friction coefficients are poorly constrained in the literature and often fitted to better reproduce the water waves for each studied case (Macias *et al.* 2021b).

Fig. 6 shows how the friction angles in the granular friction law (eq. 16) change the simulated waves (here we set $m_f = 0$ and $n = 0$). As the friction angles fitted in HySEA to reproduce SHALTOP deposit are higher than the laboratory derived friction angles, the granular flow simulated with these fitted angles is slower, leading to smaller amplitude of the first water wave whatever the studied case. A difference of maximum 20 and 10 per cent is observed in the wave amplitude for the immersed and dry entering water case, respectively. In the immersed case, the waveform is better reproduced with the fitted friction coefficients at the closest gauge 1 while this is the contrary at gauge 2. In the dry entering water case, the wave amplitude is closer to observation with non-fitted friction angles at the closest gauge even though the simulated wave is substantially underestimated in the case of granular flow entering water at 45° slope (Figs 6g and h).

Figs 7 and A11 show the influence of the friction coefficients on both the water wave and the granular avalanche for $n \in [0, 0.1]\,\mathrm{m}^{-1/3}$ s and $m_f \in [0, 1]\,\mathrm{m}^{-1}$.

When varied between 0 and 0.1, which seems to be an upper bound in the literature, the Manning coefficient n has almost no impact on the granular avalanche or on the first generated waves (see Fig. A11 for the wave). Its effect is still small but higher on the second and third waves. As there is no value that improves the results in all the configurations, we arbitrarily chose the intermediate value $n = 0.05\,\mathrm{m}^{-1/3}$ s. Note that Escalante *et al.* (2019) used $n = 0.01\,\mathrm{m}^{-1/3}$ s for water/glass friction. In our case, as glass beads are glued to the bottom surface, this coefficient should be higher.

The friction coefficient m_f between the water and granular layers slightly impacts the water wave and the avalanche when its value is higher than 0.1 (Fig. 7). As m_f increases, it decreases the wave amplitude in the immersed cases (Figs 7a and b) and increases it in the dry flow entering water cases (Figs 7c and d), probably because of the increased coupling between the entering mass and the water column. The wave amplitude is changed by a maximum of 7 per cent for $m_f = 1\,\mathrm{m}^{-1}$ compared to $m_f = 0\,\mathrm{m}^{-1}$. In the immersed case, depending on the times and gauges, the simulated waves are slightly better either with m_f lower than 0.1 or with m_f higher than 0.1. In the dry flow entering water case, the results seem better for values of m_f higher than 0.1. Concordant results are obtained for the avalanche run-out that is better for high values of m_f in the dry flow entering water case and for smaller values for the immersed case. Note here that other dissipation terms such as pressure drag or added mass effects would also have an influence, but they are beyond the scope of this paper. We thus arbitrary choose $m_f = 0.1\,\mathrm{m}^{-1}$, a value compatible with Gonzalez-Vida *et al.* (2019).

4.2.2 Hydrostatic versus non-hydrostatic water wave

When considering the hydrostatic simulation for the fully immersed or dry flow entering water cases, the maximum wave heights generated by a granular collapse on a 35° slope are overestimated by the hydrostatic HySEA simulations (Fig. A4). Moreover, depending on which
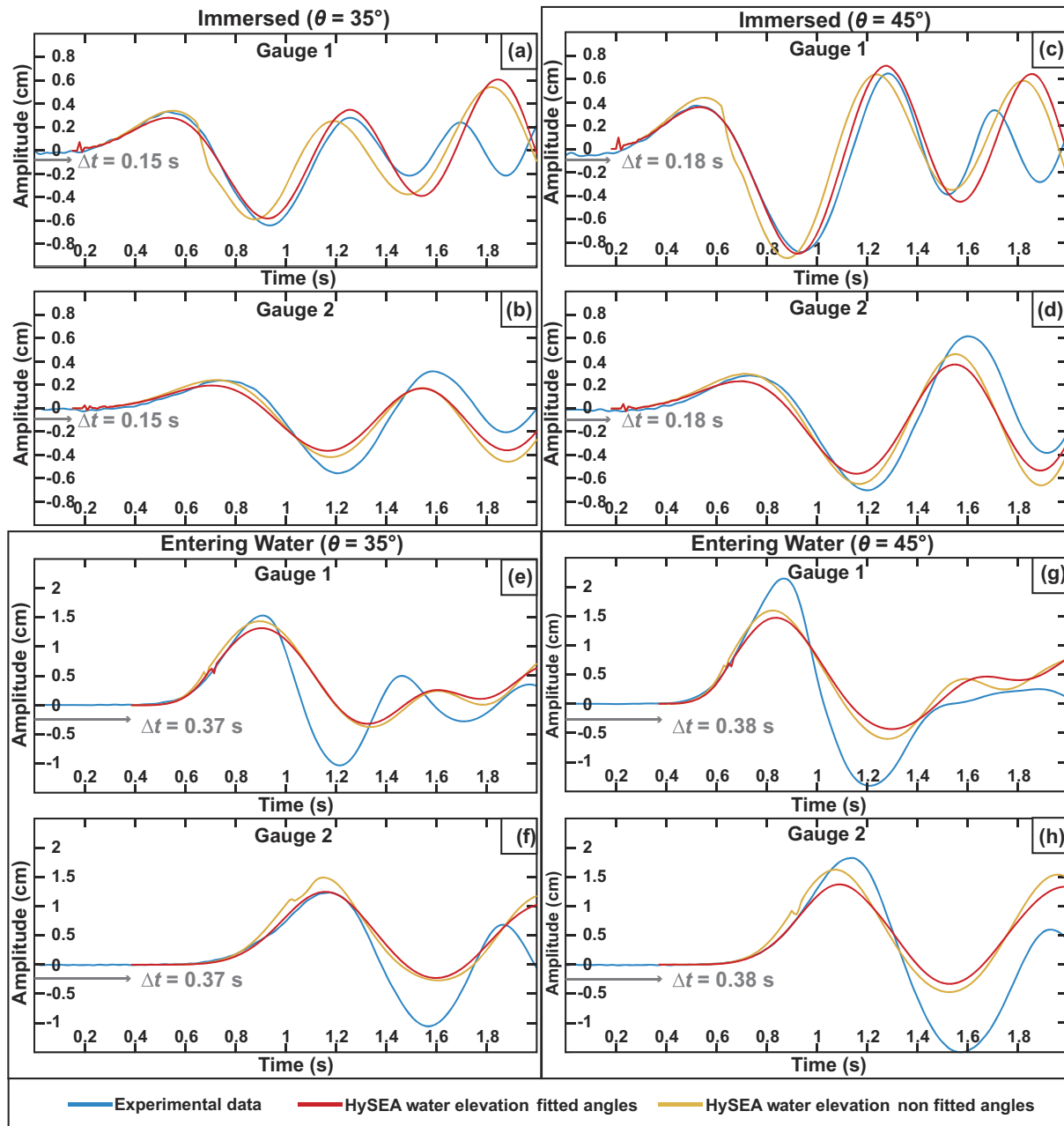
Figure 6. Impact of the fit of the friction angles (δ_1, δ_2, δ_3) used in the Pouliquen & Forterre (2002) friction law on the simulated water wave at gauges 1 (a, c, e, g) and 2 (b, d, f, h) for the non-hydrostatic HySEA in the immersed and dry entering water cases at 35° and 45° slopes. The blue lines represents the experiments and the red and yellow lines the simulations with fitted and non-fitted friction angles, respectively. Simulation waves have been synched in time to the experiment. The time-shift Δt is represented by the grey arrow.

wave is taken into account to define the maximum amplitude, the error compared to the experiments can vary from a 25 to 100 per cent. Overall, hydrostatic simulations strongly overestimate the first wave and underestimate the following troughs and waves, as is well known in the literature (Ma *et al.* 2015). On the other hand, when considering the non-hydrostatic version of the numerical model, the simulations give a much better representation of the wave amplitude and wavelength with an error varying from 10 to 25 per cent.

As an example, for the immersed case at 35°, the hydrostatic simulation overestimates waves by up to 100 per cent for the maximum amplitude and the trough is underestimated by more than 100 per cent. The non-hydrostatic simulation gives a good to very good approximation of the first waves for the immersed and dry flow entering water cases at both gauges. The maximum difference between simulated and measured waves is obtained in the dry flow entering water case where the first simulated wave is underestimated by 15 per cent. The same behaviour is obtained on a 45° slope (Fig. A5).

As stated in Section 2.1, the hydrostatic approximation has been shown to be practically applicable for kH lower than about 0.35. In the experiments simulated here, kH is always higher than 3, extending up to >10. As a result, even the non-hydrostatic simulations with the
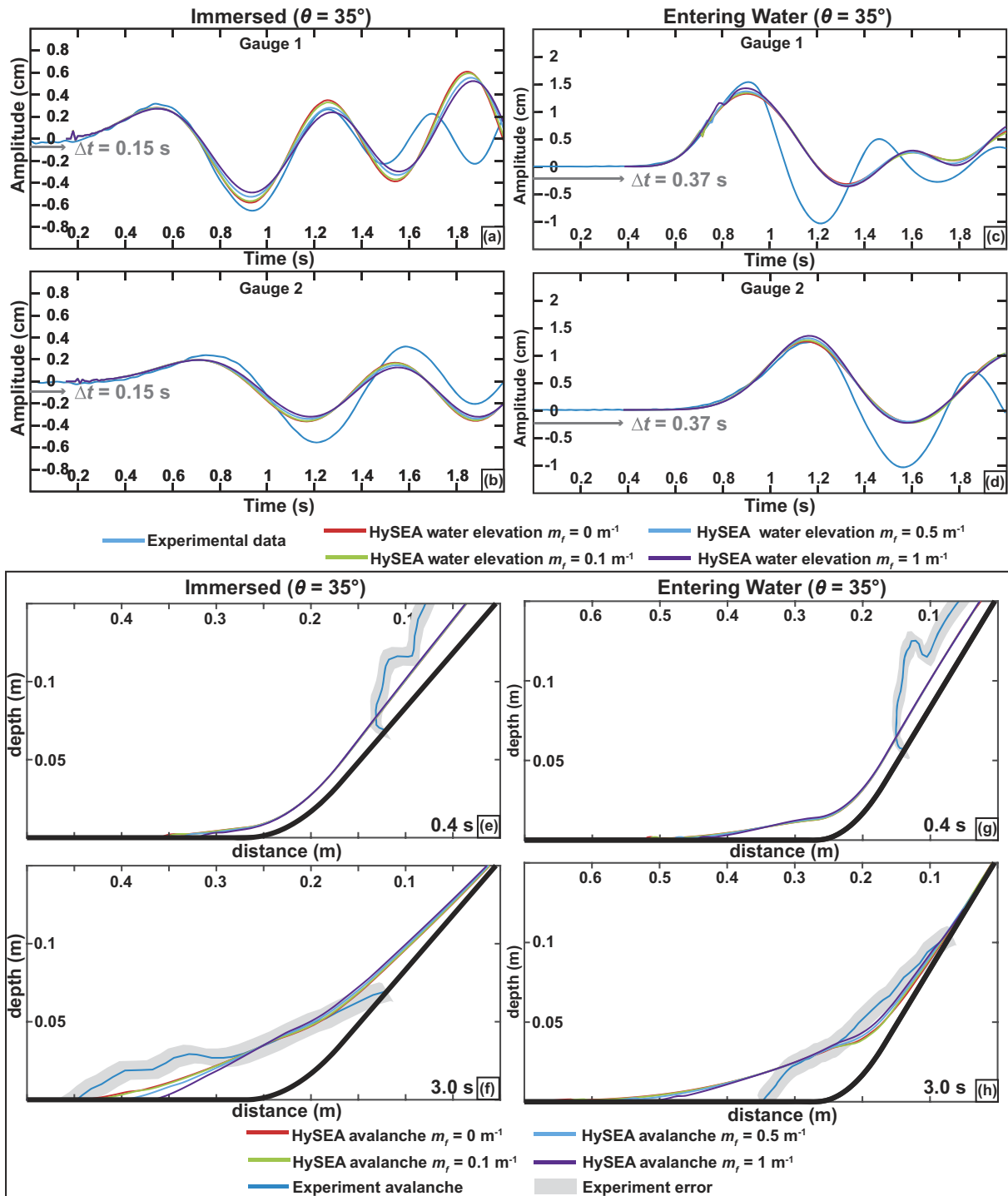
Figure 7. Impact of the avalanche/water friction coefficient (m_f) on the evolution of the free surface from the experiments and the simulations at gauges 1 (a, c) and 2 (b, d) for the non-hydrostatic HySEA simulations with a fitted friction coefficient for a 35° slope configuration. Simulation waves have been synched in time to the experiment. The time-shift Δt is represented by the grey arrow. Impact of the avalanche/water friction coefficient (m_f) on the evolution of an avalanche on a 35° slope for immersed (e,f) (Experiment 2 in Table 1) and dry flow entering water (g, h) (Experiment 3 in Table 1) configurations. The blue lines are the evolution of the water free surface of the experiments. The red, green, light blue and purple lines represent the evolution of the water free surface of the simulations.

HySEA one-layer model are not always in their validity range (Macias *et al.* 2021a). This is in particular the case in the generation area where small wavelengths are generated (Figs A6f–h and j–k, A8f–h and j–k). However, our simulations show that theses waves are still confined in the generation area during the simulation and only slightly pollute the longer wavelength waves recorded further away at the gauges. Indeed, non-hydrostatic simulations reproduce relatively well the waveforms at the gauges despite these spurious waves trapped in the generation area.

Consequently, the comparison between simulations and laboratory experiments demonstrates the limitation of the codes and makes it possible to quantify, in simple situations, the error in the calculated granular flow and deposits and in the generated water wave. With an estimate of the error, it is possible to better interpret the simulation of geological events, in particular in view of quantifying the associated hazards. Let us now compare the hydrostatic and non-hydrostatic approximation of the water layer in the natural context of the Montagne Pelée volcano (Martinique).

5 APPLICATION TO A GEOLOGICAL CASE: INSIGHT INTO MONTAGNE PELÉE LANDSLIDES AND GENERATED WAVES

5.1 Geological description and data preparation

5.1.1 Flank-collapse history and unrest at Montagne Pelée volcano

Martinique is located in the central part of the Lesser Antilles Arc. Volcanic activity on Martinique covers a period from the early Miocene to present. Montagne Pelée volcano in northern part of Martinique is an explosive-type active volcano that has experienced numerous magmatic and phreatic eruptions including the 1902–1905 and 1929–1932.

During the last 130 Ma years, three flank collapses reshaped the western part of the Montagne Pelée volcano (Fig. 8a) with volumes estimated from 1.8 km^3 for the last event at 36 ka BP (DAD3) to 25 km^3 for the oldest event (Le Friant *et al*. 2003a; Boudon *et al*. 2007; Le Friant *et al*. 2015, 2019, Brunet *et al*. 2016, Solaro *et al*. 2020). The volcanic debris-avalanche component of these landslide deposits is restricted to proximal areas and tends to stop at the break in slope in the bathymetry whereas the distal part of the landslide deposit, called SLD (Submarine Landslide Deposit), results from widespread failures of pre-existing low topographic gradient seafloor sediments (Le Friant *et al*. 2013, 2015, 2019). In Fig. 8(a), DAD3 is the debris avalanche deposit related to the last flank-collapse event (36 ka) whereas the morphological bulge (the three blue lines) result from the accumulation of the two older debris avalanche deposits related to the two older flank-collapse events (Brunet *et al*. 2016; Le Friant *et al*. 2015, 2019). The dynamics of these debris avalanches and their deposits remain unclear. Brunet *et al*. (2017) discussed the landslide dynamic by modelling the emplacement of DAD3 using SHALTOP and HySEA models. They performed sensitivity tests with SHALTOP and HySEA and concluded that large flank collapses (about 20 km^3) probably occurred in several events with successive volumes smaller than 5 km^3 entering the sea. In their simulations, they did not took into account the presence of an erodible bed, the precise reconstruction of the topography and the variation of the friction angle with collapsed volumes.

The last magmatic eruption produced a large lava dome inside an explosive crater that was excavated in the lava dome from the 1902–1905 eruption. The 1929–1932 lava dome was built on the border of the summit caldera (Cratère de l'Etang Sec). Its prominent talus slope extends to the south several hundred metres below the rim. The activity of Montagne Pelée volcano decreased significantly after the end of the last eruption in 1932 (Fig. 8b). Fumarole activity has stopped since 1970. However, since April 2019, volcanic seismic activity has been increasing. In November 2020, the OVSM-IPGP recorded a new marked increase in the seismicity and the appearance of long-period earthquakes and volcanic tremors (OVSM-IPGP 2020-2021). Observation at the end of December 2020 of a zone of degraded vegetation on the southeastern flank of Mount Pelée has suggested that diffuse CO_2 of magmatic origin may be degassing. These observations reflect an increase in the activity of the hydrothermal system of Montagne Pelée. However, the OVSM-IPGP has not recorded any evidence of large-scale deformation or high-temperature sulfur gas emission.

In this context of reactivation, the past flank-collapse history of Montagne Pelée, that is its structure with the last dome of 1929 located within and overlapping the rim of the Etang Sec caldera, with a steep non-buttressed talus slope rising nearly 800 m above the surrounding topography, could favour instability, as observed on other volcanoes (Harnett *et al*. 2019). Such failure could depressurize the magmato-hydrothermal system, trigger laterally directed explosions (blasts) and generate the emplacement of potentially tsunamigenic debris avalanches. To conduct a preliminary assessment of this problem with a numerical simulation of failure, we first perform sensitivity tests on the collapsed volumes (by adapting the friction angles used with volumes) based on the current geological knowledge of Montagne Pelée volcano. We also test the effects of an erodible substratum. These sensitivity tests allow us to provide a range of run-out distances and sea surface elevations as a function of the different collapsed volumes. We then investigate two (non-exhaustive) deterministic scenarios of potential collapse (1929 Dome scenario and Dome slope scenario) related to the current heightened seismicity and volcanic unrest (Fig. 8).

5.1.2 Collapse scenarios and data preparation

The stability of Montagne Pelée volcano is difficult to assess because of the lack of geotechnical data. To perform sensitivity tests and calibrate the model, we use the geometric and geological constraints of the three large flank-collapses identified on Montagne Pelée volcano to define the scars and volumes of the collapse scenarios (Le Friant *et al*. 2003a, b; Brunet *et al*. 2016, 2017). To reconstruct pre- and post-topography of Montagne Pelée volcano, we use the topography provided by IGN and the bathymetry collected during the AGUADOMAR expedition (Deplus *et al*. 2001). The topography and bathymetry were combined to build a 100 m resolution Digital Terrain Model (DTM). The DTM was modified to reconstruct the topography before the flank collapses by replacing the submarine deposits with a smooth slope. This DTM was then modified to reconstruct the pre- and post-topography for different volumes ranging from 1.8 to 16.2 km^3 (Fig. 9a). Note that in this
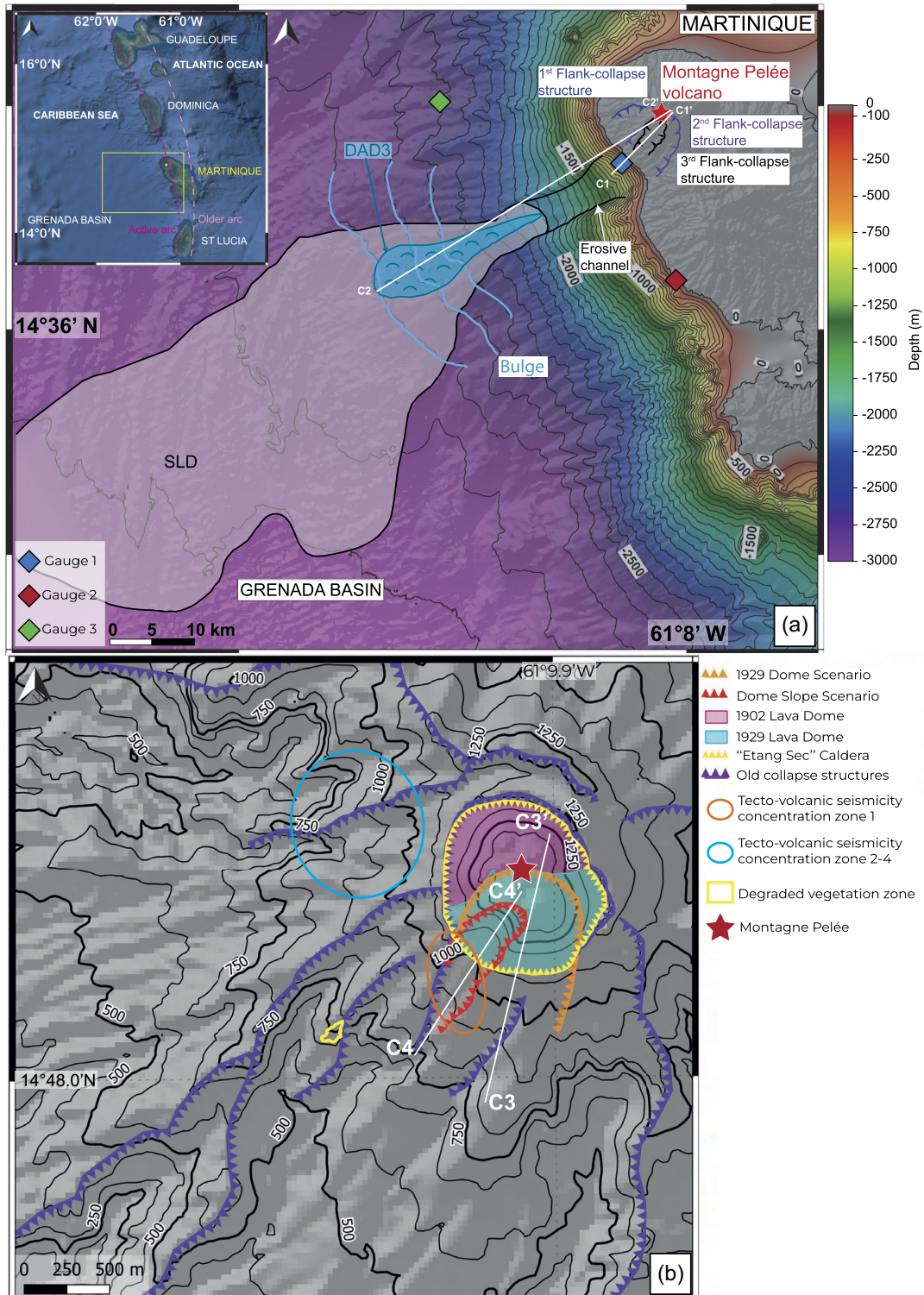
Figure 8. (a) Terrestrial digital elevation model (from IGN) with Montagne Pelée volcano (red star) and bathymetric map from the AGUADOMAR (1999) and CARAVAL (2002) cruises, adapted from Brunet *et al.* (2017). The three horseshoe-shaped structures are represented on land (Le Friant *et al.* 2003a, b). The extents of submarine landslide deposits are plotted with black lines from Brunet *et al.* (2016). The debris avalanche deposit DAD3 related to the last flank collapse event is in blue and the three blue contour lines represent the bulge associated with older debris avalanche deposits (associated with older flank collapses). The three diamonds represent the position of the gauges used to monitor the sea surface elevation generated by the debris avalanches. Inset: Lesser Antilles Arc map on the left-hand side, with Martinique Island and both the active arc (red dotted line) and older arc (orange dashed line), (figure adapted from Brunet *et al.* (2017)). (b) Terrestrial digital elevation model (from IGN) showing the Montagne Pelée volcano and the old flank-collapse structures in purple. The two lava domes of 1929 and 1932 are indicated (pink and blue) inside the 'Etang Sec' caldera (yellow line). The two potential flank-collapse scenarios related to the reactivation of the volcano are indicated with horseshoe-shaped structures in red and orange. The areas of ongoing seismic activity are contoured in blue and orange and the degraded vegetation area is contoured in yellow.
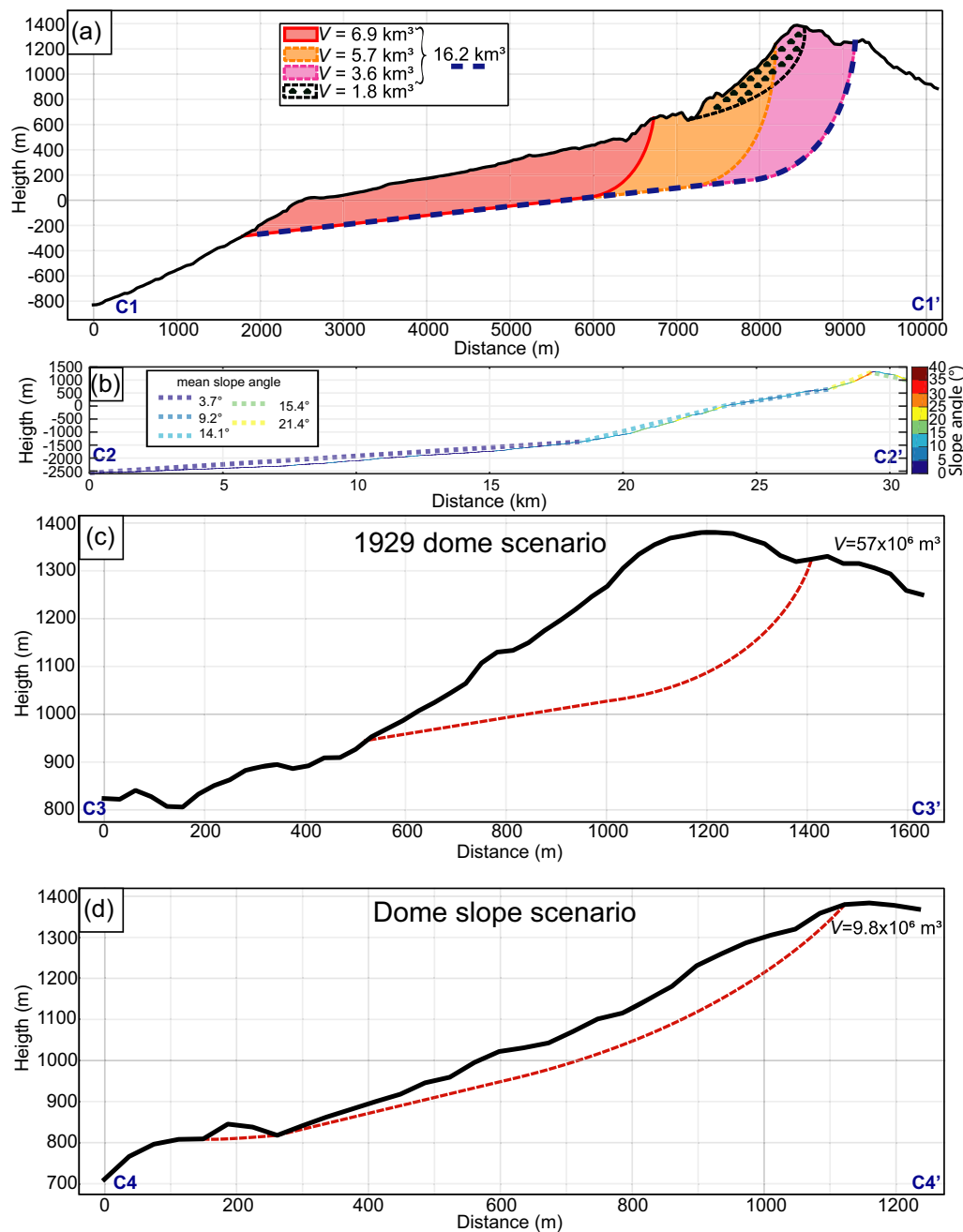
Figure 9. (a) Collapse geometries of scenarios with different volumes for the sensitivity tests. (b) Slope variations along a profile crossing the volcano and submarine flanks. The mean slope angle is shown with dotted lines averaged along sections between five main slope breaks. (c) Geometry of the 1929 Dome scenario. (d) Geometry of the Dome slope scenario.

study, the reconstruction of the first event result in an estimated volume of 16.2 km³ for the largest event, which is a bit smaller than the estimation of Le Friant *et al*. (2003a). The reconstruction of the pre-event topography was done using the isolines from the area of the volcano outside the collapse scar. Four different flank collapse scenarios involving volumes of (a) 1.8 km³, (b) 16.2 km³ and (c) 1.8 km³ subdivided into three successive subevents of 0.6 km³, and (d) 16.2 km³ subdivided into three successive subevents of 6.9 km³, 5.9 km³ and 3.7 km³, have been investigated.

Finally, to provide a first assessment of the potential instability of the edifice in the context of the unrest at Montagne Pelée since 2019, we focus our attention on the 1929–1932 lava dome located within the summit caldera. Given the current unrest conditions related to the location of volcano-tectonic seismicity and the zone of damaged vegetation, we consider that the scenario involving the partial collapse of the 1929–1932 dome is the most critical to investigate and to model (Fig. 8b). We consider two scenarios. The first scenario concerns the 1929–1932 lava dome (1929 Dome scenario) with an estimated volume of 57×10^6 m³. The second scenario concerns the collapse of part of the dome slope (Dome slope scenario, estimated volume 9.8×10^6 m³; Figs 8b, 9c and d). We use a 30 m resolution DTM provided by

Table 2. Main characteristics, friction angles and results of the simulated scenarios for volcano landslides at Montagne Pelée.

SHALTOP		Volume (km^3)	Run-out distance (km)	Offshore distance (km)	Covered surface (km^2)	Deposit maximum thickness (m)	Friction angles $\delta_1, \delta_2, \delta_3$ (°)
Single events							
-		1.8	39.4	33.4	184.2	29.3	2, 12, 4
HySEA		Volume (km^3)	Run-out distance (km)	Offshore distance (km)	Covered surface (km^2)	Deposit maximum thickness (m)	Friction angles $\delta_1, \delta_2, \delta_3$ (°)
Single events							
-		0.01	2.5	0	3.4	8.8	4.7, 14.7, 6.7
-		0.05	10.3	4.5	22.5	48	3.7, 13.7, 5.7
-		0.6	26.5	21.4	122.5	29	2.4, 12.4, 4.4
-		1.2	31.3	26	168.6	30.1	2.1, 12.1, 4.1
-		1.8	38.6	32.9	343.4	28.3	2, 12, 4
-		6.9	39.3	33.3	522.4	51.2	1.4, 11.4, 3.4
-		12.8	46.5	41.3	782.1	54.9	1.1, 11.1, 3.1
-		16.2	50.4	44.4	1105.7	53.3	0.9, 10.9, 2.9
Successive subevents (erodible deposits)							
1.8 km^3	subevent 1	0.6	26.5	21.4	122.5	29	2.4, 12.4, 4.4
	subevent 2	0.6	27.7	22.5	148.1	33.3	2.4, 12.4, 4.4
	subevent 3	0.6	29.2	23.5	183.3	44.6	2.4, 12.4, 4.4
16.2 km^3	subevent 1	6.9	39.3	33.3	522.4	51.2	1.4, 11.4, 3.4
	subevent 2	5.9	41.3	35.3	673	57.7	1.4, 11.4, 3.4
	subevent 3	3.7	41.4	35.4	688.3	69.9	1.6, 11.6, 3.6
Successive subevents (non-erodible deposits)							
1.8 km^3	subevent 1	0.6	26.5	21.4	122.5	29	2.4, 12.4, 4.4
	subevent 2	0.6	27	21.5	133.5	43	2.4, 12.4, 4.4
	subevent 3	0.6	28	22.3	155.2	53	2.4, 12.4, 4.4
16.2 km^3	subevent 1	6.9	39.3	33.3	522.4	51.2	1.4, 11.4, 3.4
	subevent 2	5.9	39.5	33.5	564	71.7	1.4, 11.4, 3.4
	subevent 3	3.7	39.6	33.6	578.9	91.3	1.6, 11.6, 3.6
Martinique unrest scenario							
Dome slope scenario		0.0098	5	0	4	27.9	4.7, 14.7, 6.7
1929 Dome scenario		0.057	13.9	8.2	33.9	57	3.7, 13.7, 5.7

IGN, the Litto3D data (IGN-SHOM) and the HOMONIM DTM provided by SHOM to reconstruct the topography and the bathymetry and perform numerical simulation.

5.2 Sensitivity tests on volumes, number of events and erodible substratum

5.2.1 Debris avalanches

The values of the friction angle to be used is still the subject of debate. Lucas's empirical law derived from dry debris avalanches (Lucas *et al*. 2011) has yielded a good fit for some volcanic contexts (Zhao *et al*. 2015) but was not able to reproduce the deposit in Martinique (Brunet *et al*. 2017) or in Guadeloupe (Perruzzeto *et al*. 2019). In these last two cases, a smaller friction coefficient was needed, suggesting that the observed greater mobility of the volcanic debris-avalanches could be explained by the presence of meteoric water, pressurized hydrothermal fluids and highly hydrothermally altered material in the sliding mass. To determine the friction angles to be used in this study, we start from the Lucas's empirical relationship (Lucas *et al*. 2011):

$$\tan(\delta) = V^{-0.0774} \tag{17}$$

and combine it with the results of Brunet *et al*. (2017), who have calibrated the angles for the 1.8 km^3 volume collapse of Montagne Pelée with geological constraints. For the 1.8 km^3, Lucas's empirical law suggests that $\delta = 11°$. However, Brunet *et al*. (2017) show that the deposits are best reproduced using $\delta = 6°$ for a Coulomb's type law, probably because of the presence of water. We therefore modify Lucas's empirical law by introducing a constant α to fit the result of Brunet *et al*. (2017):

$$\tan(\delta) = \alpha V^{-0.0774} \tag{18}$$

with $\alpha = 0.54$.

We then deduced the δ angles for each volume reported in Table 2. Given that Brunet *et al*. (2017) reproduced the 1.8 km^3 collapse of Montagne Pelée with $\delta = 6°$ for the Coulomb friction law and with $\delta_1 = 2°$, $\delta_2 = 12°$ and $\delta_3 = 4°$ for the Pouliquen and Forterre friction law,
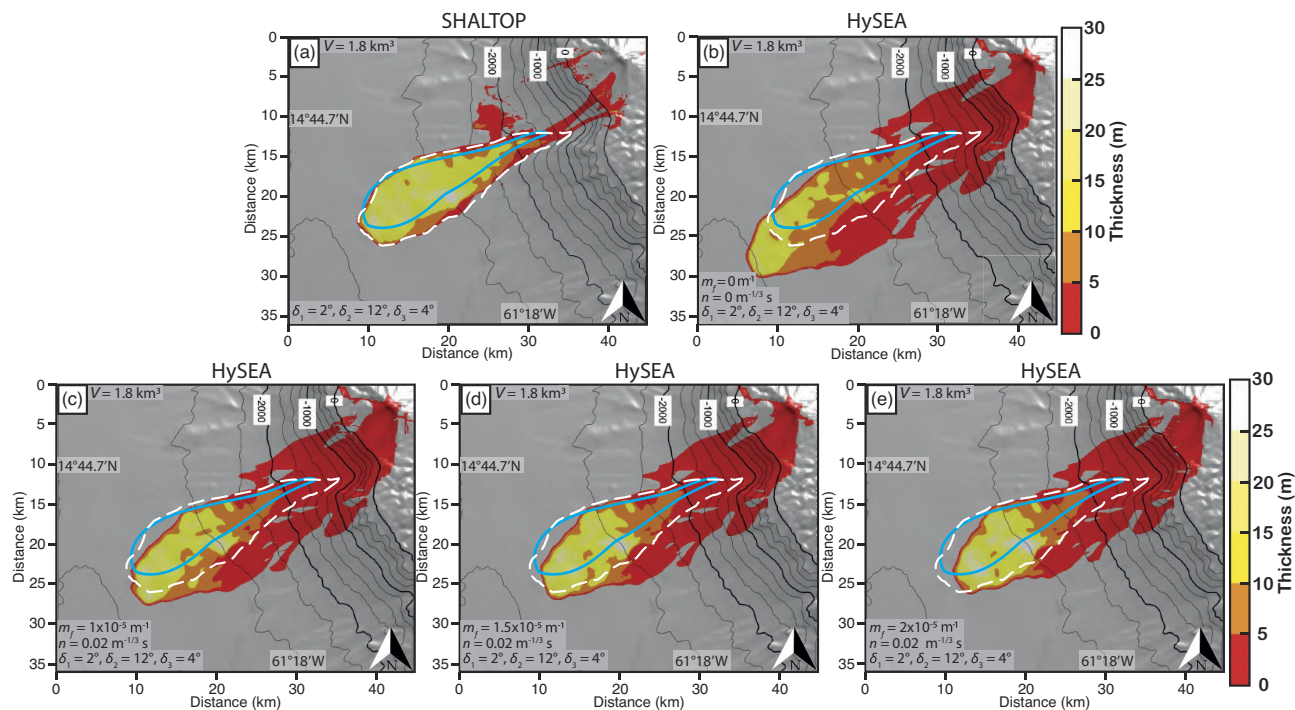
Figure 10. Final deposits calculated for the 1.8 km³ flank collapse with (a) the SHALTOP model and (b–e) the HySEA model. m_f represents the drag coefficient between the water and the granular avalanche and n is the Manning coefficient. Blue lines represent DAD3 observed on the submarine flank of the volcano. Dashed white lines represent the result of the simulation conducted by Brunet *et al.* (2017).

we calculate δ_1 from equation (18) by imposing:

$$\delta_1 = \delta - 4° \tag{19}$$

and calculate δ_2 and δ_3 using the formula defined in Section 4.1. All the angles used in the series of simulations are reported in Table 2.

In this section, we first test the influence of one single event versus multiple-stage events and the influence of a potential erodible substratum using the friction angles defined previously.

Single slide events To compare HySEA and SHALTOP for the 1.8 km³ flank collapse, we use the following angles: $\delta_1 = 2°$, $\delta_2 = 12°$ and $\delta_3 = 4°$, and we first set to zero the friction between the water and granular layer and the Manning coefficient in HySEA (Figs 10a and b). SHALTOP gives a more accurate representation of the deposit while the run-out distance using HySEA is longer. As seen from the experiment, when the slope is smaller than 15–20°, (here the average slope is about 7.6°, Fig. 9b), we do not have to fit the friction angle in HySEA to get closer to the deposit obtained with SHALTOP. Here, we then just introduce a drag in HySEA between the water and granular layer with a coefficient (m_f) and the Manning coefficient (n). We used a Manning coefficient $n = 0.02$ m$^{-1/3}$ s since our laboratory-scale study showed that it barely affects the water wave and even less the granular flow (Fig. A11). We test different values of the drag coefficient $m_f = 1 \times 10^{-5}$, 1.5×10^{-5}, 2×10^{-5} m^{-1} (Figs 10c, d and e). Note that the drag coefficient m_f has dimension of m^{-1} so that its value at the field scale should be about 10^{-3} smaller than its the laboratory-scale value. Including a drag coefficient of 1.5×10^{-5} m^{-1} and a Manning coefficient of 0.02 m$^{-1/3}$ s, we obtain the best deposit with a run-out distance similar to the observed deposit (Fig. 10d). We then compare the flow dynamics between SHALTOP ($\delta_1 = 2°$, $\delta_2 = 12°$ and $\delta_3 = 4°$) and HySEA ($\delta_1 = 2°$, $\delta_2 = 12°$ and $\delta_3 = 4°$ with a friction coefficient and a Manning coefficient of 0.02 and 1.5×10^{-5}), respectively. With SHALTOP, most of the volume of the slide initially flows rapidly downslope in the horseshoe structure, then to the coastline and offshore (Fig. A12a). A relatively small part of the slide spreads to the north whereas the main part of the slide bounces off the south side of a pre-existing erosive channel. The maximal run-out distance, reached after 300 s, is 33.4 km from the coastline (Fig. A12c). When the front stops, some material is still moving at the back of the front. This material then accumulates in the front and centre of the deposits and a tail develops behind the main mass at between 300 and 600 s (Figs A12c and d). As expected, the results are similar even though the flow simulated with SHALTOP is slightly faster (Figs A12a–h). The maximum thickness of material reaches 29.3 and 28.3 m for SHALTOP and HySEA, respectively, which is coherent with observations from Le Friant *et al.* (2003a, b). Results from numerical simulations using SHALTOP and HySEA confirms that HySEA can be used as it gives a good run-out estimation of the flow. Note however that SHALTOP better reproduces the detailed morphology of the deposit with HySEA displaying a larger spreading of the deposits on the steep submarine slopes (Figs A12e–h). We use HySEA in the following section.

To investigate additional scenarios other than the 1.8 km³ event, we use HySEA to calculate the run-out distances for 7 volumes (ranging from small flank collapse volumes to the largest volume reconstructed on Montagne Pelée volcano): $V = 10 \times 10^6$ m³, $V = 50 \times 10^6$ m³, $V = 0.6$ km³, $V = 1.2$ km³, $V = 6.9$ km³, $V = 12.8$ km³, $V = 16.2$ km³, (Fig. 11). The debris avalanche related to the smallest event
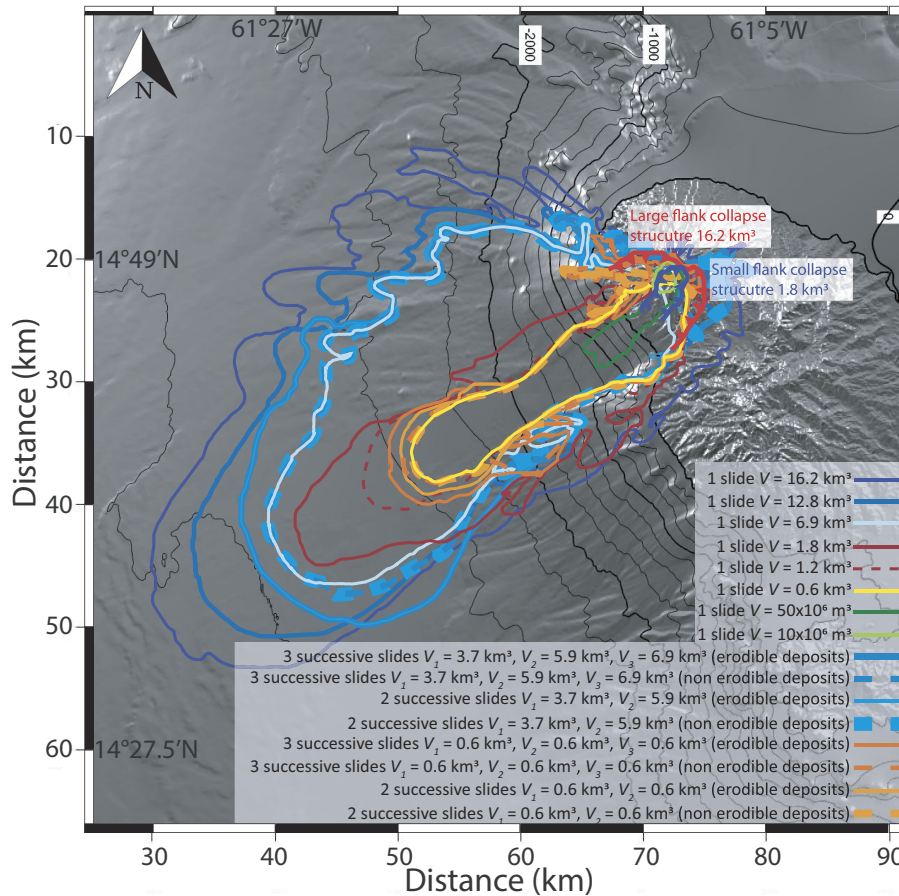
Figure 11. Final deposits pathways and extensions simulated with the HySEA model for all the sensitivity tests on Montagne Pelée.

$(10 \times 10^6 \text{ m}^3)$ does not reach the sea. The debris avalanche associated with the $50 \times 10^6 \text{ m}^3$ enters the sea and propagates over a distance of 2 km after the coastline. The 0.6 km³ event deposit stopped at 21.4 km after the coastline. The dynamics of the 6.9 km³ event are similar to those of the 16.2 km³ event presented afterwards but with a smaller run-out distance of 33.3 km after the coastline and covering an area of 522.4 km². Finally, a maximum run-out distance of 41.3 km after the coastline is obtained for a flank collapse of 12.8 km³. Regarding the flow dynamics of the debris avalanche associated with the largest volume (16.2 km³), most of the material of the slide flows rapidly downslope to the southwest in the horseshoe structure and then to the coastline and offshore (Figs A13a and b). The avalanche continues to flow, creating one main location of deposition (purple arrow in Fig. A13d) located at the front of the flow. A part of the material stays within the structure. The debris avalanche reaches a maximum run-out distance of 44.4 km from the coastline (Table 2) and a maximum deposit thickness of about 53.3 m. These results are not in agreement with the observations as the bulge (three blue lines in Fig. 8a), related to the debris-avalanche deposits associated with the event, is located 35 km from the coastline.

One slide event versus three subslide events To test the effect of a flank-collapse occurring in successive retrogressive subevents as suggested by Brunet *et al*. (2017), the 1.8 and 16.2 km³ volumes were each divided in three smaller volumes that slide one after the other, but the values of the friction angle were modified for each volume, contrary to the previous work of Brunet *et al*. (2017; Table 2).

First, for the 1.8 km³ volume, we investigate the influence of the nature of the substratum (erodible or not) on the flow dynamics and deposit. Two sets of simulations were performed considering each previous deposit either as an erodible substratum or as a solid topography for the following event. The parameters used are summarized in Table 2. For the erodible case, Fig. A14 shows: (i) a yellow dashed line delimiting the extent of the deposit resulting from the first subevent simulation (0.6 km³) with a run-out distance of 21.4 km from the coastline after 3000 s, (ii) a green dotted line delimiting the extent of the deposit resulting from the second subevent simulation (0.6 km³) with a run-out distance of 22.5 km from the coastline after 3000 s and (iii) a coloured area representing the deposit resulting from the third subevent of 0.6 km³ after 250 s. Figs A14a and b show that the third debris avalanche spreads above the previous deposit forming an erosion/deposition wave as observed for laboratory-scale dry granular flow experiments (Pouliquen & Forterre 2002; Mangeney *et al*. 2007b; Edwards *et al*. 2017; Viroulet *et al*. 2019) and for field-scale simulations (Moretti *et al*. 2012, their fig. 2d). The wave propagates beyond the front of the previous deposit, increasing the run-out distance (23.5 km from the coastline; Figs A14a, c and e). For the non-erodible substratum situation, the dynamics are different and no erosion/deposition waves are observed for the second or third subevents. The material just accumulates on the top of the thickest part (Figs A14b, d and f) and the run-out distances are smaller.
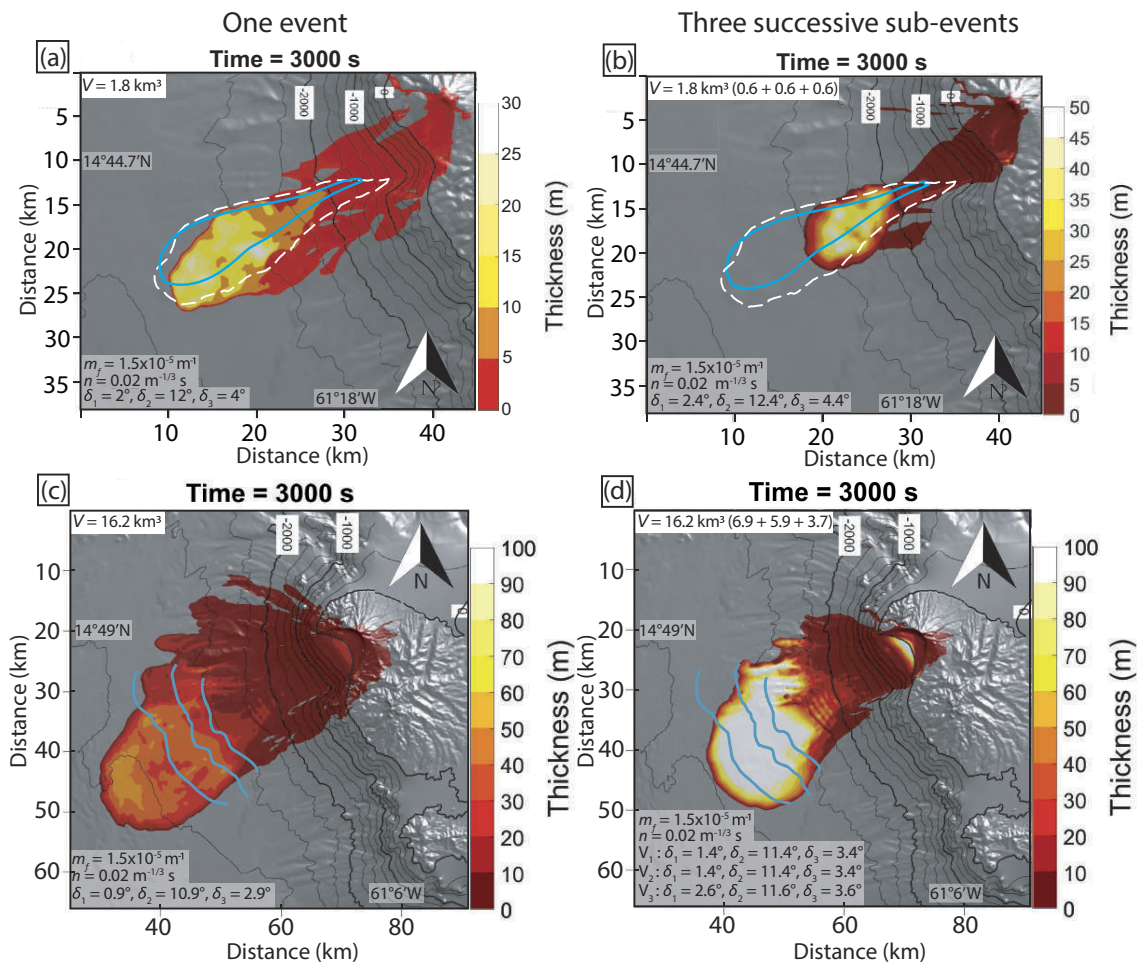
Figure 12. Final simulated deposits of the 1.8 km³ collapse scenario occurring in (a) one single event or (b) three successive subevents. Blue lines represent the observed DAD3 associated with the last flank collapse event of Montagne Pelée. Dashed white lines represent the result of the simulation conducted by Brunet *et al.* (2017). Final deposit of the 16.2 km³ collapse scenario occurring in (c) one event or (d) three successive subevents (6.9 km³, 5.9 and 3.7 km³, with erodible deposits). Blue contour lines represent the observed bulge limits indicating the maximum run-out distance of the 16.2 km³ flank collapse events at Montagne Pelée (Brunet *et al.*2017).

In both cases (erodible or non-erodible), the final run-out distance for the 1.8 km³ flank-collapse occurring in three smaller subevents is shorter than the observed deposit (blue line in Figs A14e, f and Table 2) suggesting that this event occurred in one single event (Figs 12a and b). We then investigate, for the erodible case, the effect of successive sub-events for the maximum volume of 16.2 km³ that we divided into three volumes (6.9, 5.9, and 3.7 km³). When considering one single event, the maximum thickness of material is located at the front of the deposit (53.3 m) and the final run-out distance is longer (44.4 km; Fig. 12c). The final run-out distance is smaller for three successive subevents (35.4 km versus 44.4 km; Fig. 12d). The three successive subevents lead to a maximum thickness of deposit located near the front (69.9 m). The dynamics are similar for the successive subevents 2 and 3 with the material spreading across the previous deposits, not really increasing the run-out distance. The best fit between the observations of the bulge and the results of the numerical simulations is obtained for three successive subevents.

These results tend to support the hypothesis, for the 16.2 km³scenario, of a large event that occurred in smaller subevents at Montagne Pelée. Therefore, the 6.9 km³ seems to be a maximum volume for any subevent, but it is possible that the 16.2 km³ flank collapse is composed of more than three even smaller subevents.

5.2.2 Generated waves

In this section, we simulate the wave generation and propagation with the hydrostatic and non-hydrostatic versions of the HySEA model for the five different flank collapse scenarios of Montagne Pelée involving volumes of 50×10^6 m³, 1.8 km³, 1.8 km³ subdivided into three successive sub-events, 16.2 km³, and 16.2 km³ subdivided into three successive subevents. Below, we detail the results of the first three scenarios and indicate systematically the values of the sea surface elevation obtained with both the hydrostatic and non-hydrostatic models as follows: value with hydrostatic model/value with non-hydrostatic model.
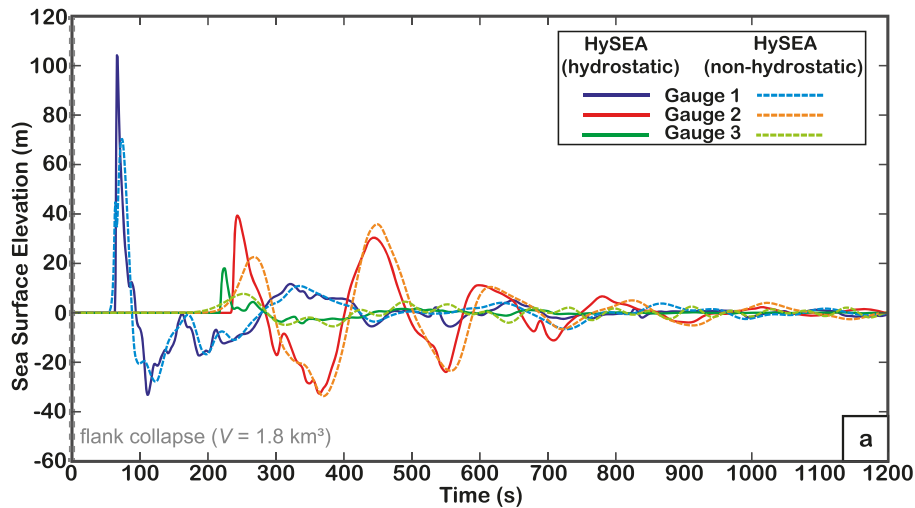
Figure 13. (a) Comparison of the sea surface elevation at three gauges calculated with the hydrostatic and non-hydrostatic versions of the HySEA model, for the case of a 1.8 km³ collapse. The gauges location are shown in Fig. 8(a).

First, the time-series of the sea surface elevation at three locations (see positions in Fig. 8a) of sea surface elevations generated by the 1.8 km³ volume occurring as a single event are shown in Fig. 13. Gauge 1 (blue), in front of the flank-collapse structure, show a maximum amplitude of 104.2 m/70.4 m for the first generated wave (Fig. 13) whereas the second (red) and third (green) gauges show a first wave of 39 m/22.6 m and 18 m/7.7 m, respectively. A second wave with an amplitude of 30 m/35.9 m is estimated at the red gauge. Using the hydrostatic model, the first wave is 32 per cent higher at gauge 1, 42 per cent higher at gauge 2 and 57 per cent higher at gauge 3, than when using the non-hydrostatic model. Using the hydrostatic and the non-hydrostatic versions of HySEA gives similar results for the avalanche part as observed in the laboratory-scale study (Section 4).

Then, waves generated by three successive flank collapses of 0.6 km³ were simulated numerically. The first subevent generated a wave of 55 m/28.9 m on the first gauge (blue), 14.5 m/7.4 m on the second gauge (red) and 4.6 m/3 m on the third gauge (green) (Fig. A15a). The second subevent resulted in larger waves (Fig. A15a). For the last 0.6 km³ subevent, the three gauges suggest waves of amplitude similar to that of the second subevent (Fig. A15a). The increasing amplitude of the waves generated by the successive events is related to their increasing velocity as the successive events start to flow higher on the slope. Note that, for the case of an erodible substratum, the wave generated by the last subevent generates a stronger wave than on a rigid substratum. The wave also displays a slightly different waveform as for instance on gauge 2 in Fig. A16.

Fig. A15(b) shows the maximum water elevation at the three gauges for the 50×10^6 m³ collapse. The gauge (blue gauge) located in front of the flank-collapse (3 km from the coast) recorded a maximum amplitude of 8 m/4.3 m for the first generated wave at 105 s (Fig. A15b). The amplitude of the first wave significantly decreases during its propagation to reach only 1 m/0.27 m and 50 cm/20 cm at the second (red) (located close to Bellefontaine) and third gauge (green) (located 20 km from the coast), respectively (Fig. A15b).

The maximum amplitude and wavelength of the generated waves for all the scenarios as a function of the volume of the event are represented in Fig. 14 for volumes varying from 50×10^6 m³ to 16.2 km³ for hydrostatic and non-hydrostatic cases. We observed that, for the case of flank collapses on La Montagne Pelée volcano, the wave amplitude increases logarithmically as a function of increasing volume whereas the wavelength increases as a function of volume according to a power law.

Typically, the calculated wavelengths λ vary from 1 km to more than 30 km. If we apply the validity criteria of the HySEA hydrostatic model ($kH < 0.314$) and of the HySEA non-hydrostatic one-layer model ($kH < 2.5$), we observe (Fig. A17) that for the shortest waves (λ = 1 km), the hydrostatic assumption is valid only within a narrow band close to coastline ($H < 55$ m) and the non-hydrostatic assumption is valid for waves propagating at depths less than 400 m. As the water depth in this case is always less than 3 km, the HySEA non-hydrostatic model is always valid for the generation/propagation of waves with wavelengths λ > 7.5 km in the calculation domain. As the avalanche deposits are located at depths less than 2.7 km, the non-hydrostatic model is always valid for the generation/propagation of waves with wavelengths λ > 6.8 km. For intermediate (15 km) and long wavelengths (30 km), the hydrostatic assumption is valid for wave propagation at depths below 850 and 1700 m, respectively.

5.3 Potential collapse scenarios related to ongoing volcano-tectonic activity

Taking into account the ongoing unrest at Montagne Pelée volcano since 2019, we considered two potential instability and collapse scenarios: the collapse of the 1929 dome with a volume of 57×10^6 m³ called the '1929 Dome scenario' and the collapse of part of the steep talus pile of the 1929 dome with a volume of 10×10^6 m³ called the 'Dome slope scenario'. Numerical simulations were performed for both scenarios using the previously calculated friction angles (Section 4.2.1). From these simulations, we estimate maximum run-out distances
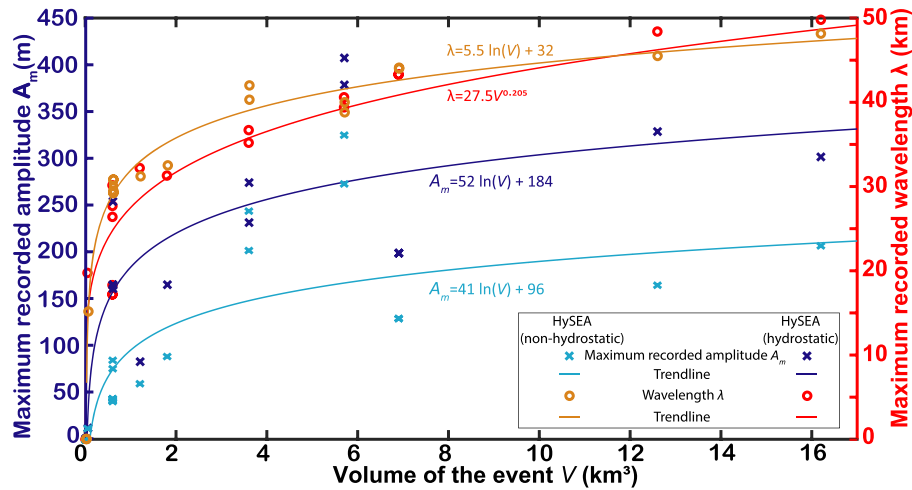
Figure 14. Maximum amplitude and wavelength of the generated waves as a function of the volume of the collapse scenarios simulated for sensitivity tests at Montagne Pelée volcano.
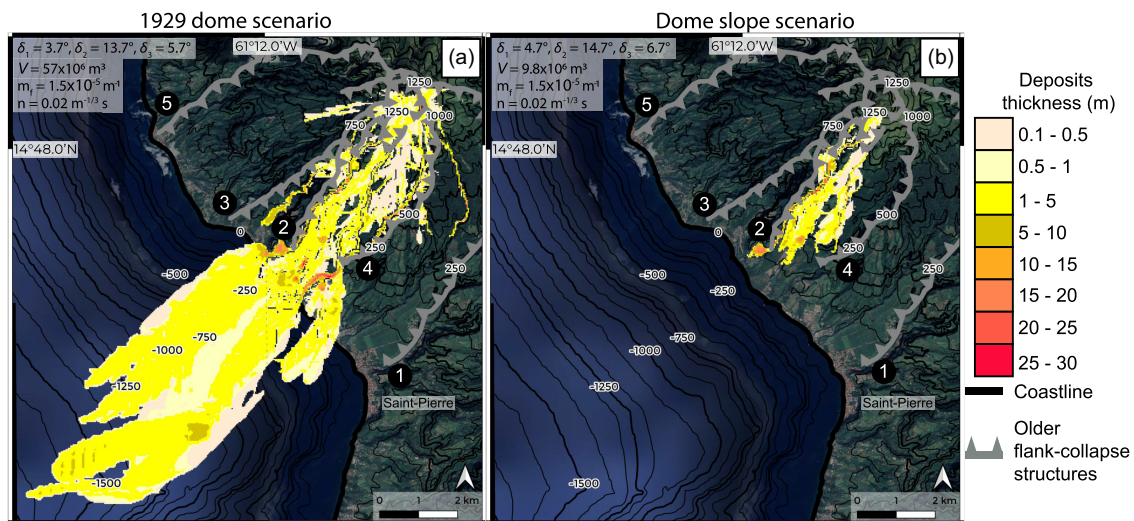

Figure 15. Final deposits calculated with HySEA for the (a) 1929 Dome collapse scenario and (b) Dome slope scenario. Older flank-collapse structures are in grey with the rims of the different structures numbered from 1 to 5.

for the deposits as displayed in Figs 15(a) and (b) for simulations with $\delta_1 = 3.7°$, $\delta_2 = 13.7°$, $\delta_3 = 5.7°$ and $\delta_1 = 4.7°$, $\delta_2 = 14.7°$, $\delta_3 = 6.7°$, respectively. In both cases (Figs 15a and b), the main part of the modelled debris avalanche flows southwest towards St Pierre. The main part of the flow is channeled between two older morphological structures that already channeled the block and ash flow deposits of the 1902–1905 and 1929–1932 eruptions, filling the Rivière Blanche valley (Le Friant *et al.* 2003a). A discontinuity (4 in Fig. 15) is formed by a cliff facing northwest on the left bank of Rivière Sèche. The rim (2 in Fig. 15a) of the structure is a continuous cliff, facing southeast on the right bank of Rivière Claire. For the 57×10^6 m³ event, part of the debris avalanche flows to the northwest, north of rim 3. The avalanche from the 1929 Dome scenario reaches 14 km (and thus 8 km from the coastline). In contrast, the avalanche from the Dome slope scenario reaches only 5.3 km from the volcano's summit, without reaching the coastline. The maximum thickness of the deposits is 30 m (1929 Dome scenario) and 27.9 m (Dome slope scenario) in valleys when channeled. The area covered by the deposits ranges from 33.9 km² for the 1929 Dome scenario and 4 km² for the Dome slope scenario. These preliminary simulations show that in both cases, an instability related to the ongoing seismic-volcanic crisis could have consequences for the population. The friction angles we used here empirically account for the presence of water as discussed in Section 5.2.1. The recent observation of damaged vegetation on the flank of the volcano suggests that the hydrothermal system is active. As on other volcanoes, both phreatic and magmatic historical eruptions at Montagne Pelée trigger the ascent and outflow of aquifer water and pressurized hydrothermal fluids in the host rock thereby increasing fluid saturation in the potentially unstable areas as well as reducing friction along low-strength listric and basal layers. In addition to the flow path of debris avalanches, the large simulated volumes of material deposited high upstream in the valleys will act as sediment sources for the genesis of intense debris flows (lahars) during torrential rainfall, often for an extended period of time following the initial collapse event (e.g. Peruzzetto *et al.* 2022). They will also act as sediment barriers allowing the formation of perched water ponds that could generate, upon dam rupture, highly damaging and mobile water waves that
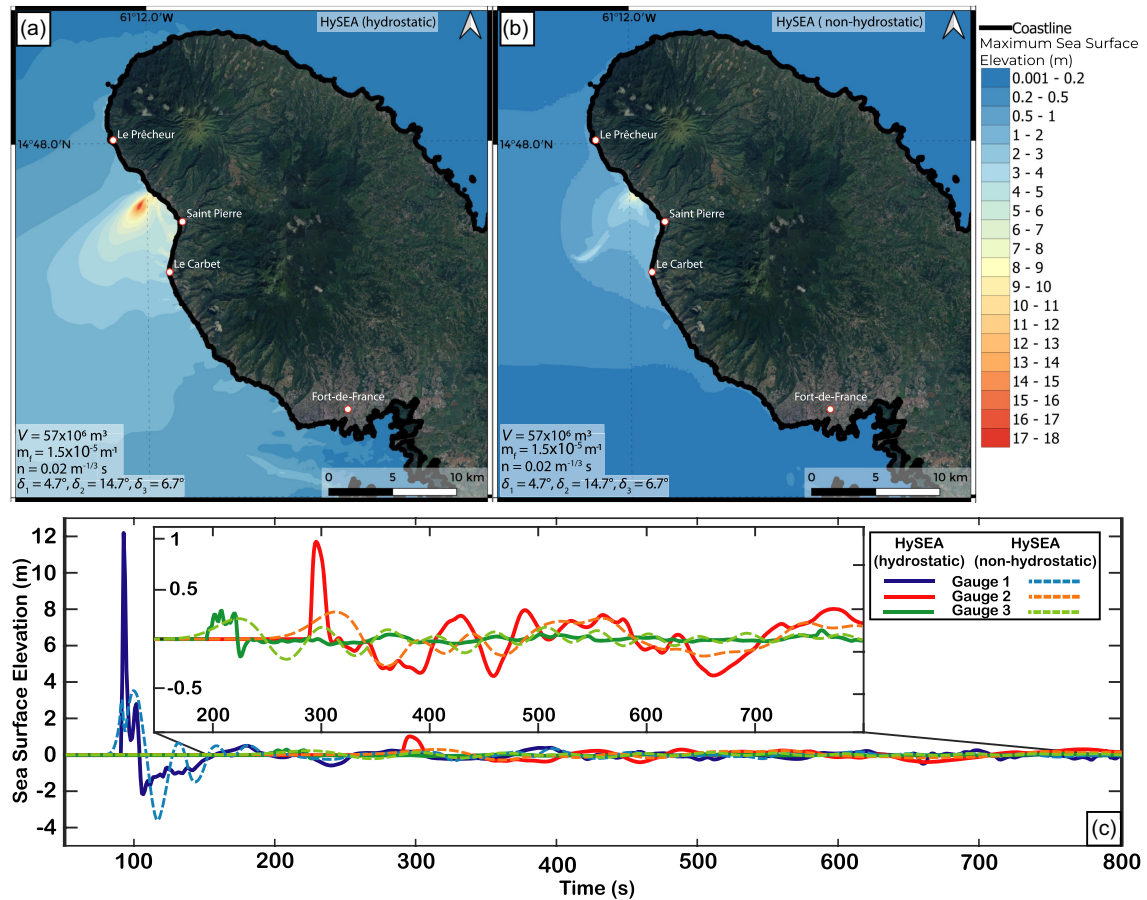
Figure 16. (a) Maximum sea surface elevation generated by the 1929 Dome scenario ($V = 57 \times 10^6$ m^3) with the hydrostatic and non-hydrostatic HySEA code and (b) evolution of the sea surface elevation at each gauge.

will propagate downstream until reaching the coastline. Depending on their characteristics, volume and flux, both the debris flows and the water surges can be potentially tsunamigenic. The resulting and potentially large submarine sediment accumulation fans can also be subject to instability and generate submarine landslide events.

Only the debris avalanche generated by the 1929 Dome scenario reaches the sea. Fig. A18 presents the evolution of the sea surface elevation using hydrostatic/non-hydrostatic versions of HySEA. The wave is generated about 100 s after the beginning of the collapse. At 150 and 200 s the waves continue to propagate from the area where the debris avalanche entered the sea. At 150 s the first wave reaches Saint-Pierre and then Le Carbet at 200 s. At 450 s, the wave is mostly dispersed and reaches Fort-de-France. Figs 16(a) and (b) show the maximum sea surface elevation for both the hydrostatic and non-hydrostatic assumption. The maximum value is recorded where the debris avalanche took place and can reach locally 18 m/8.9 m. The gauge (blue gauge) located in front of the flank-collapse structure (2 km from the coast) indicates a maximum amplitude of 12.2 m/3.5 m for the first generated wave at 92 s (Fig. 16b). The amplitude of the first wave significantly decreases during its propagation to reach only 1 m/0.29 m and 30 cm/22 cm at the second (red) (located close to Bellefontaine) and third gauge (green) (located 20 km from the coast), respectively (Figs 16c and b).

We have to keep in mind that in this study, we consider only the sea surface elevation due to the tsunami. For the future, a one-way nested grid approach should be used to obtain a realistic simulation of the flooding (10 m resolution) in terms of the extension, water depth (sea surface elevation—bottom elevation) and currents to better assess the impact on land for the population and infrastructures. Given the ongoing seismo-volcanic unrest, additional numerical simulations should be performed and the range of flooding height (inundation depth) on land should be calculated.

6 CONCLUSION

In this study, we have quantified the error of the HySEA shallow-water model in simulations of dry, immersed and dry entering water granular flows and associated tsunami. This was done by comparing HySEA results to laboratory experiments and to the SHALTOP shallow-water model that better describes topography effects. In particular, we show that topography and non-hydrostatic effects can be crucial. By artificially increasing the friction coefficients in HySEA in non-hydrostatic simulations, it is possible to take topography effects into account empirically. In this way, we were able to satisfactorily reproduce deposits from laboratory experiments as well as waves at a distance of more than two

to three times the characteristic dimension of the slide. The error in water waves ranges from 1 to 25 per cent depending on the scenario. Application to the geological case helped us better understand how past flank collapses of Montagne Pelée generated the deposits observed at sea. Although the complex dynamics of the flow are not well captured, the simulated final deposit for the 1.8 km³ event was in good agreement with field measurements. As expected, even though a lot of parameters affect the dynamics of the flow, the ability to accurately take into account the effect of a varying topography in the simulation is a key point to obtain deposits that are consistent with the observed data. This explains why SHALTOP was able to better reproduce the observed deposit. As expected, and confirmed by the numerical simulations, the volume of the event and the presence of an erodible substratum drastically affect the run-out distance and the shape of the deposits. Our analysis, based on a comparison of the deposits measured at sea and the deposits obtained from numerical simulations, shows that large a flank collapse of Montagne Pelée probably occurred as several smaller sub-events, drastically reducing the tsunami hazard around the volcano. Comparison between the hydrostatic and non-hydrostatic HySEA models shows that taking non-hydrostatic effects into account is essential at the laboratory-scale, completely changing the water waves, that is in line with a broad set of previous findings in landslide tsunami science. For the field applications chosen here, non-hydrostatic effects still change the amplitude of the first wave significantly as well as, to a lesser extent, the following wave trains. But, our results have revealed the limits of the models, in particular for short wavelengths waves ($\lambda < 1$ km) for which the hydrostatic assumption is only valid within a narrow band close to the coastline (depth < 50 m) and the non-hydrostatic assumption only valid where ocean depth is less than 400 m. Sensitivity tests performed on Montagne Pelée provided a range of run-out distances and maximum sea surface elevations for various volumes from a small collapse volume of 10×10^6 m³ to the largest collapse volumes of 16.2 km³. In terms of hazard assessment, our preliminary work is particularly important in the context of the ongoing seismic volcanic unrest at La Montagne Pelée since 2019 (OVSM-IPGP 2019-2021) that could favour gravitational instabilities. Future work should focus on a more realistic simulation of the flooding, that is, the propagation of the tsunami inland, which was not done here.

As a result, even though actual models are able to provide the order of magnitude of the generated waves, lots of issues should be investigated and quantified to better describe the dynamics of landslide-generated tsunamis. While this study points towards model limitations related to topography effects in depth-averaged models, granular dilatation/compression, complex processes during granular impact with the water, description of in-depth variations and validity domain of the models, there are lots of other possible improvements linked for example to better description of grain–water interaction or hydrodynamic resistance.

ACKNOWLEDGMENTS

DATA AVAILABILITY

Experimental data are accessible via the following Zenodo link: https://zenodo.org/record/7337193#.Y39IIXbMJhF, with the doi: 10.5281/zenodo.7337193.

REFERENCES

Abadie, S. M., Harris, J. C., Grilli, S. T. & Fabre, R., 2012. Numerical modeling of tsunami waves generated by the flank collapse of the Cumbre Vieja Volcano (La Palma, Canary Islands): tsunami source and near field effects. *J. geophys. Res.,* **117**(C5), doi:10.1029/2011JC007646.

Abadie, S., Morichon, D., Grilli, S. & Glockner, S., 2008. VOF/Navier-Stokes numerical modeling of surface waves generated by subaerial landslides, *La Houille Blanche,* **1**, 21–26.

Abadie, S., Morichon, D., Grilli, S. & Glockner, S., 2010. Numerical simulation of waves generated by landslides using a multiple-fluid Navier–Stokes model. *Coastal Eng.,* **57**, 779–794.

Barrett, R., *et al.*, 2019. Revisiting the tsunamigenic volcanic flank collapse of Fogo Island in the Cape Verdes, offshore West Africa, *Geol. Soc., Lond., Spec. Publ.,* **500**, 13–26.

Behrens, J., *et al.*, 2021. Probabilistic tsunami hazard and risk analysis: a review of research gaps, *Front. Earth Sci.,* **9**, doi:10.3389/feart.2021.628772.

Bouchut, F., Fernández-Nieto, E. D., Koné, E. H., Mangeney, A. & Narbona-Reina, G., 2017. A two-phase solid-fluid model for dense granular flows including dilatancy effects: comparison with submarine granular collapse experiments, *EPJ Web Conf.,* **140**, doi:10.1051/epjconf/201714009039.

Bouchut, F., Fernández-Nieto, E. D., Mangeney, A. & Narbona-Reina, G., 2016b. A two-phase two-layer model for fluidized granular flows with dilatancy effects, *J. Fluid Mech.,* **801,** 166–221.

Bouchut, F., Fernandez-Nieto, E., Kone, E., Mangeney, A. & Narbona-Reina, G., 2021. Dilatancy in dry granular flows with a compressible $\mu(I)$ rheology, *J. Comput. Phys.,* **429,** doi:10.1016/j.jcp.2020.110013.

Bouchut, F., Ionescu, I. R. & Mangeney, A., 2016a. An analytic approach for the evolution of the static/flowing interface in viscoplastic granular flows, *Commun. Math. Sci.,* **14,** 2101–2126.

Bouchut, F., Mangeney-Castelnau, A., Perthame, B. & Vilotte, J.-P., 2003. A new model of Saint Venant and Savage–Hutter type for gravity driven shallow-water flows, *Compt. Rend. Math.,* **336,** 531–536.

Bouchut, F. & Westdickenberg, M., 2004. Gravity driven shallow water models for arbitrary topography, *Commun. Math. Sci.,* **2,** 359–389.

Boudon, G., Friant, A. L., Komorowski, J.-C., Deplus, C. & Semet, M. P., 2007. Volcano flank instability in the Lesser Antilles Arc: diversity of scale, processes, and temporal recurrence, *J. geophys. Res.,* 112(B8), doi:10.1029/2006JB004674.

Bougouin, A., Paris, R. & Roche, O., 2020. Impact of fluidized granular flows into water: implications for tsunamis generated by pyroclastic flows, *J. geophys. Res.,* **125,** e2019JB018954.

Bougouin, A., Roche, O., Paris, R. & Huppert, H. E., 2021. Experimental insights on the propagation of fine-grained geophysical flows entering water, *J. geophys. Res.,* **126,** e2020JC016838.

Brunet, M., *et al.*, 2016. Composition, geometry, and emplacement dynamics of a large volcanic island landslide offshore Martinique: from volcano flank-collapse to seafloor sediment failure?, *Geochem., Geophys., Geosyst.,* **17,** 699–724.

Brunet, M., Moretti, L., Friant, A. L., Mangeney, A., Nieto, E. D. & Bouchut, F., 2017. Numerical simulation of the 30–45 ka debris avalanche flow of Montagne Pelée volcano, Martinique: from volcano flank collapse to submarine emplacement, *Nat. Hazards,* **87,** 1189–1222.

Castro, M. J., Ferreiro, A. M., Garcı´a-Rodrı´guez, J. A., González-Vida, J. M., Macı´as, J., Parés, C. & Vázquez-Cendón, M. E., 2005. The numerical treatment of wet/dry fronts in shallow flows: application to one-layer and two-layer systems, *Math. Comput. Model.,* **42,** 419–439.

Christen, M., Kowalski, J. & Bartelt, P., 2010. RAMMS: numerical simulation of dense snow avalanches in three-dimensional terrain, *Cold Reg. Sci. Technol.,* 63(1-2), 1–14.

de Haas, T., Braat, L., Leuven, J. R., Lokhorst, I. R. & Kleinhans, M. G., 2015. Effects of debris flow composition on runout, depositional mechanisms, and deposit morphology in laboratory experiments, *J. geophys. Res.,* **120,** 1949–1972.

Delannay, R., Valance, A., Mangeney, A., Roche, O. & Richard, P., 2017. Granular and particle-laden flows: from laboratory experiments to field observations, *J. Phys. D: Appl. Phys.,* 50(5), doi:10.1088/1361-6463/50/5/053001.

Delgado-Sánchez, J. M., Bouchut, F., Fernández-Nieto, E. D., Mangeney, A. & Narbona-Reina, G., 2020. A two-layer shallow flow model with two axes of integration, well-balanced discretization and application to submarine avalanches, *J. Comput. Phys.,* **406,** doi:10.1016/j.jcp.2019.109186.

Denlinger, R. P. & Iverson, R. M., 2004. Granular avalanches across irregular three dimensional terrain: 1. Theory and computation, *J. geophys. Res.,* 109(F1), doi:10.1029/2003JF000085.

Deplus, C., *et al.*, 2001. Submarine evidence for large-scale debris avalanches in the Lesser Antilles Arc, *Earth planet. Sci. Lett.,* **192,** 145–157.

Edwards, A. N. & Gray, J. M., 2014. Erosion–deposition waves in shallow granular free-surface flows, *J. Fluid Mech.,* **762,** 35–67.

Edwards, A. N., Russell, A. S., Johnson, C. G. & Gray, J. M., 2019. Frictional hysteresis and particle deposition in granular free-surface flows, *J. Fluid Mech.,* **875,** 1058–1095.

Edwards, A. N., Viroulet, S., Kokelaar, B. P. & Gray, J. M., 2017. Formation of levees, troughs and elevated channels by avalanches on erodible slopes, *J. Fluid Mech.,* **823,** 278–315.

Escalante, C., Dumbser, M. & Castro., M.J., 2019. An efficient hyperbolic relaxation system for dispersive non-hydrostatic water waves and its solution with high order discontinuous Galerkin schemes, *J. Comput. Phys.,* **394,** 385–416.

Favreau, P., Mangeney, A., Lucas, A., Crosta, G. & Bouchut, F., 2010. Numerical modeling of landquakes, *Geophys. Res. Lett.,* **37,** doi:10.1029/2010GL043512.

Fernández-Nieto, E. D., Bouchut, F., Bresch, D., Dı´az, M. J. & Mangeney, A., 2008. A new Savage–Hutter type model for submarine avalanches and generated tsunami, *J. Comput. Phys.,* **227,** 7720–7754.

Fernandez-Nieto, E. D., Garres-Diaz, J., Mangeney, A. & Narbona-Reina, G., 2016. A multilayer shallow model for dry granular flows with the mu(I) rheology: application to granular collapse on erodible beds, *J. Fluid Mech.,* **798,** 643–681.

Fernandez-Nieto, E.D., Garres, J., Mangeney, A. & Narbona-Reina, G., 2018. 2D granular flows with the mu(I) rheology and side walls friction: a well balanced multilayer discretization, *J. Comp. Phys.,* **356,** 192–219.

Fine, I. V., Rabinovich, A. B., Bornhold, B. D., Thomson, R. E. & Kulikov, E. A., 2005. The Grand Banks landslide-generated tsunami of November 18, 1929: preliminary analysis and numerical modeling, *Mar. Geol.,* **215,** 45–57.

Fine, I. V., Rabinovich, A. B., Thomson, R. E. & Kulikov, E. A., 2003. Numerical modeling of tsunami generation by submarine and subaerial landslides, in *Dans Submarine Landslides and Tsunamis,* pp. 69–88, Springer.

Fischer, J.-T., Kowalski, J. & Pudasaini, S. P., 2012. Topographic curvature effects in applied avalanche modeling, *Cold Reg. Sci. Technol.,* **74-75,** 21–30.

Garres-Díaz, J., Fernández-Nieto, E. D., Mangeney, A. & de Luna, T. M., 2020. A weakly non-hydrostatic shallow model for dry granular flows, *J. Sci. Comput.,* **86,** doi:10.1007/s10915-020-01377-9.

George, D. L., Iverson, R. M. & Cannon, C. M., 2017. New methodology for computing tsunami generation by subaerial landslides: application to the 2015 Tyndall Glacier landslide, Alaska. *Geophys. Res. Lett.,* **44,** 7276–7284.

Gittings, M. L., 1992. SAIC's adaptive grid Eulerian code. *DNA Numerical Methods Symposium Defense Nuclear Agency*.

Glimsdal, S., Pedersen, G. K., Harbitz, C. B. & Løvholt, F., 2013. Dispersion of tsunamis: does it really matter?, *Nat. Hazards Earth Syst. Sci.,* 13(6), 1507–1526.

González-Vida, J., Macias, J. Castro, M. J. Sánchez-Linares , C. Asunción, M. & Ortega, S. 2019. The Lituya Bay landslide-generated mega-tsunami. Numerical simulation and sensitivity analysis., *Nat. Hazards and Earth Syst. Sci.,* (), doi:10.5194/nhess-2018-224.

Green, A. & Naghdi, P., 1976. A derivation of equations for wave propagation in water of variable depth, *Fluid Mech.,* **78,** 237–246.

Grilli, S. T., *et al.*, 2014. Modeling of SMF tsunami hazard along the upper US East Coast: detailed impact around Ocean City, MD, *Nat. Hazards,* **76,** 705–746.

Gylfadóttir, S. S., *et al.*, 2017. The 2014 Lake Askja rockslide-induced tsunami: optimization of numerical tsunami model using observed data, *J. geophys. Res.,* 122(5), 4110–4122.

Harnett, C. E., *et al.*, 2019. Presentation and analysis of a worldwide database for lava dome collapse events: the Global Archive of Dome Instabilities (GLADIS), *Bull. Volcanol.,* **81,** doi:10.1007/s00445-019-1276-y.

Heinrich, P., Mangeney, A., Guibourg, S., Roche, R., Boudon, G. & Cheminée, J.-L., 1998. Simulation of water waves generated by a potential debris avalanche in Montserrat, Lesser Antilles. *Geophys. Res. Lett.,* **25,** 3697–3700.

Horrillo, J., Wood, A., Kim, G.-B. & Parambath, A., 2013. A simplified 3-D Navier-Stokes numerical model for landslide-tsunami: application to the Gulf of Mexico, *J. geophys. Res.,* **118,** 6934–6950.

Ionescu, I.R., Mangeney, A., Bouchut, F. & Roche, R., 2015. Viscoplastic modeling of granular column collapse with pressure-dependent rheology, *J. Non-Newton. Fluid Mech.,* **219,** 1–18.

Iverson, R. M. & George, D. L., 2014. A depth-averaged debris-flow model that includes the effects of evolving dilatancy. I. Physical basis, *Proc. R. Soc., A,* **470**(2170), doi:10.1098/rspa.2013.0819.

Iverson, R. M. & Ouyang, C., 2015. Entrainment of bed material by Earth-surface mass flows: Review and reformulation of depth-integrated theory, *Rev. Geophys.,* **53,** 27–58.

Jiang, L. & LeBlond, P. H., 1992. The coupling of a submarine slide and the surface waves which it generates, *J. geophys. Res.,* **97**(C8), 12731–12744.

Kelfoun, K., 2011. Suitability of simple rheological laws for the numerical simulation of dense pyroclastic flows and long-runout volcanic avalanches, *J. geophys. Res.,* **116**(B8), doi:10.1029/2010JB007622.

Kelfoun, K., Giachetti, T. & Labazuy, P., 2010. Landslide-generated tsunamis at Réunion Island, *J. geophys. Res.,* **115**(F4), doi:10.1029/2009JF001381.

Kelfoun, K. & Vargas, S. V., 2015. VolcFlow capabilities and potential development for the simulation of lava flows, *Geol. Soc., Lond., Spec. Publ.,* **426,** 337–343.

Kim, J., Løvholt, F., Issler, D. & Forsberg, C. F., 2019. Landslide material control on tsunami genesis—the Storegga Slide and tsunami (8100 y BP), *J. geophys. Res.,* **124,** 3607–3627.

Kirby, J. T., *et al.*, 2022.Validation and inter-comparison of models for landslide tsunami generation, *Ocean Modell.,* **170,** doi:10.1016/j.ocemod.2021.101943.

Kirby, J., Wei, G., Chen, Q., Kennedy, A. & Dalrymple, R., 1998. Funwave 1.0: Fully Nonlinear Boussinesq Wave Model - Documentation and User's Manual, Research report No. CACR-98-06, Hydraulic Engineering Reports.

Lane, E. M., Mountjoy, J. J., Power, W. L. & Mueller, C., 2016. Probabilistic hazard of tsunamis generated by submarine landslides in the Cook Strait Canyon (New Zealand), in *Global Tsunami Science: Past and Future,* Vol. I, pp. 3757–3774, Birkhäuser.

Le Friant, A., Boudon, G., Deplus, C. & Villemant, B., 2003a. Large scale flank collapse events during the activity of Montagne Pelée, Martinique, Lesser Antilles. *J. geophys. Res.,* **108**(B1), doi:10.1029/2001JB001624.

Le Friant, A., *et al.*, 2013. Expedition 340: Preliminary Report, Integrated Ocean Drilling Program, doi:10.2204/iodp.pr.340.2012.

Le Friant, A., *et al.*, 2019. Submarine Landslides Around Volcanic Islands, in *Submarine Landslides: Subaqueous Mass Transport Deposits from Outcrops to Seismic Profiles,* Chapter 17, Geophysical Monograph Series, pp. 277–297, eds Ogata, Kei, Festa, Andrea & Pini, Gian Andrea, American Geophysical Union.

Le Friant, A., Heinrich, P., Deplus, C. & Boudon, G, 2003b. Numerical simulation of the last flank-collapse event of Montagne Pelée, Martinique, Lesser Antilles, *Geophys. Res. Lett.,* **30**(B1), doi:10.1029/2001JB001624.

Le Friant, A., Ishizuka, O., Boudon, G., Palmer, M. R., Talling, P. J., Villemant, B. & Watt, S. F., 2015. Submarine record of volcanic island construction and collapse in the Lesser Antilles arc: first scientific drilling of submarine volcanic island landslides by IODP Expedition 340. *Geochem., Geophys., Geosyst.,* **16,** 420–442.

Le Méhauté, B., 1976. *An Introduction to Hydrodynamics and Water Waves,* Springer-Verlag, viii + 323 p.

Løvholt, F., Glimsdal, S. & Harbitz, C. B.(2020). On the landslide tsunami uncertainty and hazard. *Landslides* **17,** 2301–2315.

Lucas, A., Mangeney, A., Mège, D. & Bouchut, F.(2011). Influence of the scar geometry on landslide dynamics and deposits: application to Martian landslides. *J. geophys. Res.,* **116,** doi:10.1029/2011JE003803.

Ma, G., Kirby, J. T., Hsu, T.-J. & Shi, F., 2015. A two-layer granular landslide model for tsunami wave generation: theory and computation, *Ocean Modell.,* **93,** 40–55.

Ma, G., Kirby, J. T. & Shi, F., 2013. Numerical simulation of tsunami waves generated by deformable submarine landslides, *Ocean Modell.,* **69,** 146–165.

Macı́as, J., Escalante, C. & Castro, M. J., 2021a. Multilayer-HySEA model validation for landslide generated tsunamis. Part I: rigid slides, in *Nat. Hazards Earth Syst. Sci.,* **21,** 775–789.

Macı́as, J., Escalante, C. & Castro, M. J., 2021b. Multilayer-HySEA model validation for landslide generated tsunamis. Part II: granular slides, *Nat. Hazards Earth Syst. Sci.,* **21,** 791–805.

Macı́as, J., *et al.* 2015. The Al-Borani submarine landslide and associated tsunami. A modelling approach, *Mar. Geol.,* **361,** 79–95.

Majd, M. S. & Sanders, B. F., 2014. The LHLLC scheme for two-layer and two-phase transcritical flows over a mobile bed with avalanching, wetting and drying, *Adv. Water Resour.,* **67,** 16–31.

Mangeney, A., Bouchut, F., Thomas, N., Vilotte, J. P. & Bristeau, M. O., 2007a. Numerical modeling of self-channeling granular flows and of their levee-channel deposits, *J. geophys. Res.,* **112**(F2), doi:10.1029/2006JF000469.

Mangeney, A., Heinrich, P. H., Roche, R., Boudon, G. & Cheminée, J. L., 2000. Modeling of debris avalanche and generated water waves: application to real and potential events in Montserrat, *Phys. Chem. Earth, A: Solid Earth Geod.,* **25,** 741–745.

Mangeney, A., Roche, O., Hungr, O., Mangold, N., Faccanoni, G. & Lucas, A., 2010. Erosion and mobility in granular collapse over sloping beds, *J. geophys. Res.,* **115**(F3), doi:10.1029/2009JF001462.

Mangeney, A., Tsimring, L. S., Volfson, D., Aranson, I. S. & Bouchut, F., 2007b. Avalanche mobility induced by the presence of an erodible bed and associated entrainment, *Geophys. Res. Lett.,* **34**(22), doi:10.1029/2007GL031348.

Mangeney-Castelnau, A., Bouchut, F., Vilotte, J. P., Lajeunesse, E., Aubertin, A. & Pirulli, M., 2005. On the use of Saint Venant equations to simulate the spreading of a granular mass, *J. geophys. Res.,* **110**(B9), doi:10.1029/2004JB003161.

Mangeney-Castelnau, A., Vilotte, J. P., Bristeau, M. O., Perthame, B., Bouchut, F., Simeoni, C. & Yernini, S., 2003. Numerical modeling of avalanches based on Saint-Venant equations using a kinetic scheme, *J. geophys. Res.,* **108**(B11), 2527–2544.

Martin, N., Ionescu, I., Mangeney, A., Bouchut, F. & Farin, M., 2017. Continuum viscoplastic simulation of a granular column collapse on large slopes: $\mu(I)$ rheology and lateral wall effects, *Phys. fluids,* **29**(1), doi:10.1063/1.4971320.

McGuire, W. J., 1996. Volcano instability: a review of contemporary themes, *Geol. Soc., Lond., Spec. Publ.,* **110,** 1–23.

Mergili, M., Fischer, J.-T., Krenn, J. & Pudasaini, S. P., 2017. r.avaflow v1, an advanced open source computational framework for the propagation and interaction of two-phase mass flows, *Geosci. Model Dev.,* **10,** 553–569.

Moretti, L., Allstadt, K., Mangeney, A., Capdeville, Y., Stutzmann, E. & Bouchut, F., 2015. Numerical modeling of the Mount Meager landslide constrained by its force history derived from seismic data, *J. geophys. Res.,* **120**(4), 2579–2599.

Moretti, L., Mangeney, A., Capdeville, Y., Stutzmann, E., Huggel, C., Schneider, D. & Bouchut, F., 2012. Numerical modeling of the Mount Steller landslide flow history and of the generated long period seismic waves, *Geophys. Res. Lett.,* **39**(16), doi:10.1029/2012GL052511.

Moretti, L., Mangeney, A., Walter, F., Capdeville, Y., Bodin, T., Stutzmann, E. & Le Friant, A., 2020. Constraining landslide characteristics with Bayesian inversion of field and seismic data, *Geophys. J. Int.,* **221**(2), 1341–1348.

OVSM-IPGP(2019-2021) Monthly bulletin, Observatoire volcanologique et sismologique de Martinique (IPGP), http://www.ipgp.fr/fr/ovsm/bilans-mensuels-de-lovsm

OVSM-IPGP(2020-2021) Weekly bulletin, Observatoire volcanologique et sismologique de Martinique (IPGP), http://www.ipgp.fr/fr/ovsm/bilans-hebdomadaires

Pailha, M. & Pouliquen, O., 2009. A two-phase flow description of the initiation of underwater granular avalanches, *J. Fluid Mech.,* **633,** 115–135.

Paris, A., Heinrich, P., Paris, R. & Abadie, S., 2020. The December 22, 2018 Anak Krakatau, Indonesia, landslide and tsunami: preliminary modeling results, *Pure appl. Geophys.,* **177**(2), 571–590.

Perttu, A., Caudron, C., Assink, J. D., Metz, D., Tailpied, D., Perttu, B. & Taisne, B., 2020. Reconstruction of the 2018 tsunamigenic flank collapse and eruptive activity at Anak Krakatau based on eyewitness reports, seismo-acoustic and satellite observations, *Earth planet. Sci. Lett.,* **541,** doi:10.1016/j.epsl.2020.116268.

Peruzzetto, M., *et al.* 2022. Simplified simulation of rock avalanches and subsequent debris flows with a single thin-layer model: application to the Prêcheur river (Martinique, Lesser Antilles), *Eng. Geol,* **296,** doi:10.1016/j.enggeo.2021.106457.

Peruzzetto, M., Komorowski, J.-C., Friant, A. L., Rosas-Carbajal, M., Mangeney, A. & Legendre, Y., 2019. Modeling of partial dome collapse of La Soufrière of Guadeloupe volcano: implications for hazard assessment and monitoring, *Sci. Rep.,* **9,** doi:10.1038/s41598-019-49507-0.

Peruzzetto, M., Mangeney, A., Bouchut, F., Grandjean, G., Levy, C., Thiery, Y. & Lucas, A., 2021. Topography curvature effects in thin-layer models for gravity driven flows without bed erosion, *J. geophys. Res.,* **126**(4), e2020JF005657, doi:10.1029/2020JF005657.

Peruzzetto, M., Mangeney, A., Grandjean, G., Levy, C., Thiery, Y., Rohmer, J. & Lucas, A., 2020. Operational estimation of landslide runout: comparison of empirical and numerical methods, *Geosciences,* **10,** 424, 1–35.

Pitman, E. B. & Lee, L., 2005. A two-fluid model for avalanche and debris flows, *Phil. Trans. R. Soc., A,* **363**(1832), 1573–1601.

Popinet, S., 2015. A quadtree-adaptive multigrid solver for the Serre–Green–Naghdi equations, *J. Comput. Phys.,* **302,** 336–358.

Pouliquen, O., 1999. Scaling laws in granular flows down rough inclined planes, *Phys. Fluids,* **11,** 542–548.

Pouliquen, O. & Forterre, Y., 2002. Friction law for dense granular flows: application to the motion of a mass down a rough inclined plane, *J. Fluid Mech.,* **453,** 133–151.

Pudasaini, S. P., 2012. A general two-phase debris flow model, *J. geophys. Res.,* **117**(F3), doi:10.1029/2011JF002186.

Pudasaini, S. P. & Mergili, M., 2019. A multi-phase mass flow model, *J. geophys. Res.,* **124**(12), 2920–2942.

Rauter, M., 2021. The compressible granular collapse in a fluid as a continuum:validity of a Navier-Stokes model with $\mu(J)$-$\Phi(J)$-rheology, *J. Fluid Mech.,* **915**(A87), doi:10.1017/jfm.2021.107.

Rauter, M., Kofler, A., Huber, A. & Fellin, W., 2018. faSavageHutterFOAM 1.0: depth integrated simulation of dense snow avalanches on natural terrain with OpenFOAM, *Geosci. Model Dev.,* **11**(7), 2923–2939.

Rauter, M. & Tukovic, Z., 2018. A finite area scheme for shallow granular flows on three-dimensional surfaces, *Comput. Fluids,* **166,** 184–199.

Rauter, M., Viroulet, S., Gylfadóttir, S. S., Fellin, W. & Løvholt, F., 2022. Granular porous landslide tsunami modelling–the 2014 Lake Askja flank collapse, *Nat. Commun.,* **13**(1), 1–13.

Robbe-Saule, M., Morize, C., Henaff, R., Bertho, Y., Sauret, A. & Gondret, P., 2021. Experimental investigation of tsunami waves generated by granular collapse into water, *J. Fluid Mech.,* **907**(A11), doi:10.1017/jfm.2020.807.

Rocha, F. M., Johnson, C. G. & Gray, J. M., 2019. Self-channelisation and levee formation in monodisperse granular flows, *J. Fluid Mech.,* **876,** 591–641.

Rondon, L., Pouliquen, O. & Aussillous, P., 2011. Granular collapse in a fluid: role of the initial volume fraction, *Phys. Fluids,* **23,** doi:10.1063/1.3594200.

Roux, S. & Radjai, F., 1997. Texture-dependent rigid plastic behavior, in *Physics of Dry Granular Media,* NATO ASI Series, Vol. 350, pp. 305–311, eds Herrmann, H.J., Hovi, J.P. & Luding, S., Kluwer.

Russell, A. S., Johnson, C. G., Edwards, A. N., Viroulet, S., Rocha, F. M. & Gray, J. M, 2019. Retrogressive failure of a static granular layer on an inclined plane, *J. Fluid Mech.,* **869,** 313–340.

Sarlin, W., Morize, C., Sauret, A. & Gondret, P., 2021. Nonlinear regimes of tsunami waves generated by a granular collapse, *J. Fluid Mech.,* **919,** doi:10.1017/jfm.2021.400.

Savage, S. B. & Hutter, K., 1989. The motion of a finite mass of granular material down a rough incline, *J. Fluid Mech.,* **199,** 177–215.

Shi, F., Kirby, J. T., Harris, J. C., Geiman, J. D. & Grilli, S. T., 2012. A high-order adaptive time-stepping TVD solver for Boussinesq modeling of breaking waves and coastal inundation, *Ocean Modell.,* **43,** 36–51.

Siebert, L., 1984. Large volcanic debris avalanches: characteristics of source areas, deposits, and associated eruptions, *J. Volc. Geotherm. Res.,* **22,** 163–197.

Solaro, C., Boudon, G., Friant, A. L., Balcone-Boissard, H., Emmanuel, L. & Paterne, M., 2020. New insights into the recent eruptive and collapse history of Montagne Pelée (Lesser Antilles Arc) from offshore marine drilling site U1401A (IODP Expedition 340), *J. Volc. Geotherm. Res.,* **403,** doi:10.1016/j.jvolgeores.2020.107001.

Tappin, D. R., 2014. Did a submarine landslide contribute to the 2011 Tohoku tsunami?, *Mar. Geol.,* **357,** 344–361.

Viroulet, S., Edwards, A. N., Johnson, C. G., Kokelaar, B. P. & Gray, J. M., 2019. Shedding dynamics and mass exchange by dry granular waves flowing over erodible beds, *Earth planet. Sci. Lett.,* **523,** doi:10.1016/j.jvolgeores.2020.107001.

Viroulet, S., Sauret, A. & Kimmoun, O., 2014. Tsunami generated by a granular collapse down a rough inclined plane, *Europhys. Lett.,* **105**(3), doi:10.1209/0295-5075/105/34004.

Williams, R., Rowley, P. & Garthwaite, M. C., 2019. Reconstructing the Anak Krakatau flank collapse that caused the December 2018 Indonesian tsunami, *Geology,* **47,** 973–976.

Yavari-Ramshe, S. & Ataie-Ashtiani, B., 2015. A rigorous finite volume model to simulate subaerial and submarine landslide-generated waves, *Landslides,* **14,** 203–221.

Yavari-Ramshe, S. & Ataie-Ashtiani, B., 2016.Numerical modeling of subaerial and submarine landslide-generated tsunami waves—recent advances and future challenges, *Landslides,* **13,** 1325–1368.

Yavari-Ramshe, S., Ataie-Ashtiani, B. & Sanders, B. F., 2015. A robust finite volume model to simulate granular flows, *Comput. Geotech.,* **66,** 96–112.

Zhang, C., Kirby, J. T., Shi, F., Ma, G. & Grilli, S. T., 2021a. A two-layer non-hydrostatic landslide model for tsunami generation on irregular topography. 1. Theoretical basis, *Ocean Modell.,* **159,** doi:10.1016/j.ocemod.2020.101749.

Zhang, C., Kirby, J. T., Shi, F., Ma, G. & Grilli, S. T., 2021b. A two-layer non-hydrostatic landslide model for tsunami generation on irregular topography. 1. Numerical discretization and model validation, *Ocean Modell.,* **160,** doi:10.1016/j.ocemod.2021.101769.

Zhao, J., *et al.*, 2015. Model space exploration for determining landslide source history from long-period seismic data, *Pure appl. Geophys.,* **172,** 389–413.

Zhou, H., Moore, C. W., Wei, Y. & Titov, V. V., 2011. A nested-grid Boussinesq-type approach to modelling dispersive propagation and runup of landslide-generated tsunamis, *Nat. Hazards Earth Syst. Sci.,* **11,** 2677–2697.

SUPPORTING INFORMATION

Supplementary data are available at *GJI* online.

Please note: Oxford University Press is not responsible for the content or functionality of any supporting materials supplied by the authors. Any queries (other than missing material) should be directed to the corresponding author for the article.